# Imaging the 2013 explosive crater excavation and new dome formation at Volcán de Colima with TerraSAR-X, time-lapse cameras and modelling

Thomas R. Walter (1), Claire E. Harnett (2), Nick Varley (3), Dulce Vargas Bracamontes (4, 5), Jacqueline Salzer (1), Edgar U. Zorn (1), Mauricio Bretón (3), Raúl Arámbula (4), Mark E. Thomas (2)

(1) GFZ German Research Center for Geosciences, Telegrafenberg, 14473 Potsdam, Germany

(2) Institute of Geophysics and Tectonics, University of Leeds, Leeds LS2 9JT, UK.

(3) Facultad de Ciencias, Universidad de Colima, Av. Bernal Díaz del Castillo #340, Col. Villas San Sebastián, C.P. 28045, Colima, México.

(4) Centro Universitario de Estudios e Investigaciones Vulcanológicas (CUEIV), Universidad de Colima, Av. Bernal Díaz del Castillo #340, Col. Villas San Sebastián, C.P. 28045, Colima, México.

(5) CONACYT-CUEIV, Universidad de Colima, Av. Bernal Díaz del Castillo #340, Col. Villas San Sebastián, C.P. 28045, Colima, México.

## Abstract

The summit region of steep volcanoes hosting lava domes often displays rapid geomorphologic and structural changes, which are important for monitoring the source region of hazards. Explosive crater excavation is often followed by new lava-dome growth, which is one of the most dynamic morphometric changes that may occur at volcanoes. However, details of these crater formations, and the ensuing new dome growth remain poorly studied. A common problem is the lack of observational data due to hazardous field access and the limited resolution of satellite remote sensing techniques. This paper describes the destructive-constructive crater activity at Volcán de Colima, Mexico, which occurred between January and March 2013. The crater geometry and early dome formation were observed through a combination of high-resolution TerraSAR-X spotmode satellite radar images and permanently installed monitoring cameras. This combined time-lapse imagery was used to identify ring-shaped gas emissions prior to the explosion and to distinguish between the sequential explosion and crater excavation stages, which were followed by dome growth. Crater formation and dome growth is first observed by the TerraSAR-X data. By means of particle image velocimetry, the digital flow field is computed from consecutive camera images, showing that vertical dome growth is dominant at the beginning. The upward growth is found to grade into spreading and a lateral growth domain. After approximately two months of gradually filling the excavated craters with new magma, the dome overflows the western margin of the crater and develops into a flow that produces block and ash flow hazards. We discuss and compare the observations to discrete element models, allowing us to mimic the vertical and lateral growth history of the dome and to estimate the maximum strength of the bulk rock mass. Moreover, our results allow a discussion on the controls of a critical dome height that may be reached prior to its gravitational spreading. This study, for the first time, provides a detailed view into explosive crater formation and new dome formation at Volcán de Colima, with important implications for other dome-building volcanoes.

***Keywords:*** *Volcán de Colima, dome growth and collapse, camera imaging, volcano monitoring, deformation*

# 1. Introduction

## 1.1. Dome-building volcanoes

Stratovolcanoes often exhibit rapidly changing eruption styles, from effusive to explosive, with a dramatically changing morphology, from construction to destruction, as vividly shown at the Shiveluch volcano in Kamchatka (Belousov et al., 1999), Mount St. Helens in the U.S. (Christiansen and Peterson, 1981), Soufrière Hills, Montserrat (Hooper and Mattioli, 2001), Merapi in Indonesia (Ratdomopurbo et al., 2013), and others (Voight, 2000). In silicic volcanoes, characterized by magma with a higher viscosity, domes are extruded when either the volatile content or ascent rate is low.

Lava domes commonly grow forming a very complex morphology within craters that are often recorded as nested and contain steep slopes. Lava domes may therefore completely fill a cratered summit region and subsequently overflow the former crater rims, leading to dynamic changes in dome growth and gradation to flow-like structures. These domes may form flows hundreds of metres to kilometres long (Fink and Anderson, 2000) that are controlled by a complex morphology, and may therefore locally accelerate or decelerate, associated with dilatation or contraction, respectively (Walter et al., 2013b). While dome growth in summit craters is often described in the literature, the morphologic evolution of a dome and its hosting cratered volcano summit has barely been conjointly investigated.

Dome-building volcanoes are rather common. More than 200 volcanoes of this type have been active worldwide in the Holocene, with over 400 dome-forming episodes since 1000 AD (Ogburn et al., 2015). In the $20^{th}$ century, a dome-building volcano has erupted almost every year on average, with more than 100 of such eruptions in the past 35 years alone (Sheldrake et al., 2016). Dome formation is often associated with explosive eruptions (Newhall and Melson, 1983), and the hazards associated with dome collapse are the formation of pyroclastic density currents (PDCs), blasts, lahars, and rock avalanches. Approximately 20% of the VEI4 and larger eruptions occurred at dome-building volcanoes, and since 1600 AD, three out of four eruptions with recorded fatalities involved dome-related hazards (Ogburn et al., 2015), underlining the particular hazard potential associated with the emplacement of summit domes. Prominent examples of large eruptions at dome-building volcanoes occurred at Mt. Pelee in 1902 (Martinique), Volcán de Colima in 1913 (Mexico), Kelut in 1919 (Indonesia), Usu in 1944 (Japan), Bezymianny in 1956 (Russia), Mount St. Helens in 1980 (USA), Chaiten in 2008 (Chile), Merapi in 2010 (Indonesia), and Volcán de Colima again in 2015. These dome erupting volcanoes share similarities, such as a steep (and difficult to access) morphology, low eruption rates (0.01-0.1 $km^3$ per year), high groundmass crystallinity, high viscosities ($10^6$ to $10^{11}$ Pa s) and high yield strength (Cashman et al., 2006). Nevertheless, many different growth mechanisms can be observed, which may largely arise from viscosity transformations (Yokoyama, 2005) and the ductile-brittle transition of magma leading to failure or healing (Castro et al., 2012). These transformations can also influence the mechanisms controlling deformation, magma ascent and finally dome extrusion (Lavallee et al., 2012).

The extrusion of domes often occurs in cratered areas, such as the summit craters of steep-sided stratovolcanoes. This location often makes it difficult to closely monitor the details of dome growth and its morphologic shaping processes. Therefore, experimental and numerical models could help to gain insights into how domes grow, spread and develop internal structures (Fink and Griffiths, 1998; Hale et al., 2009a), and provide insight into observed surface textures (Husain et al., 2014). According to Husain and co-authors, variations in material stiffness and strength are important in the development of different morphological characteristics in lava domes.

Various modern monitoring techniques have been applied at lava domes with the aim of understandign their dynamics, growth and instability. These techniques include seismicity (Reyes-Davila et al., 2016), gravimetry and magnetism (Portal et al., 2016), muography (Nishiyama et al., 2017), satellite TIR (Carr et al., 2016), InSAR (Salzer et al., 2017), radar amplitude (Chaussard, 2017), infrared time-lapse (Walter et al., 2013a), terrestrial laser scanning (Dalfsen et al., 2017), drone photogrammetry (Darmawan et al., 2018), and fixed camera observations (Salzer et al., 2017). Many of these previous studies aimed to interpret sequential stages of growth and collapsing lava domes. A special research focus has been placed on the physics and rheology in the conduit that are associated with the destruction of lava domes (Huppert et al., 1982; Fink and Griffiths, 1998; Lavallee et al., 2012). Despite all these advances, very basic details of dome growth, lateral spread, instability and formation in developing summit craters are poorly monitored. Eyewitness accounts are still one of the most important sources of information available for recent eruptions (Saucedo et al., 2010). At a number of domes, repeat analogue photographs and video recordings enabled monitoring of their morphology (Yamashina et al., 1999; Major et al., 2008; Vallance et al., 2008; Walter et al., 2013b). The observations support our fundamental understanding of how domes grow and develop a complex and variable morphology and provide parameters for modelling (Hale et al., 2009a; Husain et al., 2014). One common difficulty is that dome-forming episodes are rarely closely observed due to hazardous access and challenging high spatial and temporal data sampling. In this work we combined time-lapse and radar observations at the 2013 Volcán de Colima dome, providing a prime example of sequential crater excavation followed by dome growth.

### 1.2. Volcán de Colima

Volcán de Colima (Figure 1) is the most active volcano in Mexico, located in the trans-Mexican volcanic belt, linked to the convergence of the Cocos and Rivera plates under the North American plate. The volcano is known for climactic (VEI 4-5) eruptions in an approximately 100-year interval (Luhr, 1981) and abundant dome extrusion episodes. Volcán de Colima has experienced numerous debris avalanches (Cortes et al., 2010), such as 4300 years ago (Luhr and Prestegaard, 1985), and poses a significant risk, as it is located near the cities of Colima (30 km) and Ciudad Guzmán (25 km). Recent eruptive episodes occurred in 1975-1976, 1981-1982, 1991-1994, 1998-1999, 2001-2003, and 2004-2005. The following dome-building phase began in 2007 and continued until mid-2011. The summit remained quiet during 2012, while the 2007-11 dome was subject to cooling and contraction (Salzer et al., 2017). Then, in early January 2013 a seismicity increase signalled the arrival of a new batch of magma from depth (Arámbula-Mendoza et al., 2018). This event was followed by a series of Vulcanian explosions on 6, 11, 13, and 29 January 2013 that reached up to 2500 m in height and caused minor pyroclastic flows travelling westward (Zobin et al., 2015; Arámbula-Mendoza et al., 2018). Later summit deformation was identified for this period (Salzer et al., 2014). Associated with these four explosions, the 2007-11 dome was deeply excavated, producing a nested cratered summit region, and complex new growth of a lava dome commenced that we could closely monitor using radar satellite and time-lapse camera records.

Volcán de Colima is probably one of the best monitored volcanoes in Latin America, with an extensive seismic network installed at the mid-to-lower volcano flanks (Arámbula-Mendoza et al., 2018), allowing the identification of eruption precursors (Lamb et al., 2017). Nevertheless, morphologic and dynamic changes in the steep-sided volcano edifice and its summit area remain difficult to determine using ground-based methods, which is why non-intrusive remote video monitoring (Bretón-Gonzalez et al., 2013), digital image correlation (Walter et al., 2013a), infrared imaging (Stevenson and Varley, 2008), oblique terrestrial and airborne photogrammetry (James and Varley, 2012; Mueller et al., 2013; Thiele et al., 2017), thermal satellite (Abrams et al., 1991) and high-resolution spot mode satellite radar observations (Salzer et al., 2014; Salzer et al., 2017) are increasingly being used. Due to the steep and rapidly changing morphology, interpreting such remote sensing data remains challenging, and information on the cratered and dome-building summit is occasionally limited (Pinel et al., 2011). As we will show in this work, by use of terrestrial photogrammetry, we are able to track the morphologic evolution of the volcano summit region in very high detail. First, fresh lava was identified on 11 January during an overflight, which started to grow as a lava dome on 14 January (Varley et al., 2019). Our records now provide more insights into the development of the nested summit craters and allow detailed quantitative measurement of dome growth and spreading.

# 2. Methods

We apply remote sensing image monitoring methods, synthetic aperture radar (SAR) and time-lapse camera analysis to measure crater excavation and dome growth. To better understand the growth rates of the domes, we then design distinct element models, allowing the explanation of non-linear vertical growth rates during dome construction. In addition, we compare our observations to the seismic records.

## 2.1. Seismic recording

The Telemetric Seismic Network of Colima (RESCO) manages and organizes the seismic monitoring of Volcán de Colima and is part of the Center for Studies and Volcanological Research (CUEIV) of the University of Colima. The seismic network and station configuration is reviewed in detail in (Arámbula-Mendoza et al., 2018). Data from a permanent broadband (Guralp CMG 6TD) seismic station are considered here for comparing our findings to an independent dataset. The SOMA station is located approximately 1.7 km away from the summit crater on the NW flank of the volcano. Data transmission is achieved by radio to Colima city, where the data processing and analysing facilities are located. The data are sampled at 100 Hz and stored at a 24-bit resolution. Averaged power spectral density estimates of overlapped, windowed signal sections were employed for the SSAM computations. A high-pass filter of 0.5 Hz was employed to minimize the oceanic microseismic noise.

## 2.2. TerraSAR-X

We consider SAR data acquired every 11 days by the German radar satellite TerraSAR-X (TSX). The specialty of TSX in the case of dome-building volcanoes is its capability to acquire data in high-resolution spotlight mode, an acquisition type yielding a spatial resolution better than 2 metres. Such a high resolution is unprecedented at most dome-building volcanoes worldwide and allows close observation of the Volcán de Colima summit region (Salzer et al., 2014). A further major advantage of the SAR technique is that it is an active sensor, which means that the ground is illuminated by the sensor, operating independent of daylight. Because of the radar wavelength, here in the X-band, the SAR signal even passes through eruption clouds, allowing close structural monitoring of the cratered landscape, which is especially useful during a volcanic crisis (Pallister et al., 2013). Acquisitions were analysed in ascending mode, with an 11-day repeat pass. The SAR data were already interferometrically processed and analysed in an earlier study (Salzer et al., 2014). Here, we not only limit the SAR data analysis to the pre-eruptive phase but also consider those SAR data that were acquired during the Vulcanian eruptions and dome growth. For this analysis, the interferometric technique is no longer valuable due to ash coverage, rapid reflectivity changes and resulting decorrelation. Therefore, we exploit the amplitude information. SAR data were stacked and coregistered to a merged photogrammetry-LiDAR dataset at a 5 m resolution (Salzer et al., 2014). Then, we first investigate the morphologic changes in the SAR amplitude data and generate composite maps, as performed at dome-building volcanoes elsewhere (Walter et al., 2015; Chaussard, 2017; Arnold et al., 2018).

The satellite actually sees the backscattered electromagnetic microwave radiation. Each reflected pixel represents the proportion of power relative to the energy scattered and transmitted back. This process naturally depends strongly on the surface geometry, which is why the local slope at the ground, relative to the satellite's incidence, can be used to identify significant variations in the morphology. Furthermore, surface roughness on the X-band length scale (wavelength of 31 mm and frequency of 9.6 GHz) and the presence of water affect the amplitude (Wadge et al., 2011).

The measured amplitude depends on the sum of all scatterers within a ground resolution pixel. In particular, the dielectric material constant controls the effective complex relative permittivity (Adams et al., 1996). Direct quantification of the components of the relative permittivity is challenging in the field, but under laboratory conditions, ash and dry and wet snow have been shown to have specific permittivity characteristics that may be studied, at least qualitatively, in the field (Arnold et al., 2018). In this work, we investigated the amplitude data from the SAR mission TerraSAR-X (TSX). Because of the high-resolution spot mode (1-2 m ground resolution), we are able to identify changes occurring in the summit of the dome. To avoid geocoding warping artefacts in the steep summit region, we analyse the amplitude in radar coordinates.

### 2.3. Time-lapse camera

Time-lapse terrestrial photographic methods are a very sophisticated and low-cost extension to other volcano monitoring methods (Major et al., 2005). Terrestrial photography with digital systems offers continuous footage at reasonable costs (Walter, 2011; Diefenbach et al., 2012) and, therefore, long-term monitoring perspectives. One of the pioneering time-lapse observations was made at the Showa-Shinzan dome on Hokkaido, Japan, in 1944-45, where the growth history was recorded by daily outline sketches from a fixed observation point (Mimatsu, 1995). This observation has become one of the best documented examples of subaerial dome growth in the world (Minakami et al., 1951; Miyamachi et al., 1987). Digital cameras have now replaced manual drawing; but similar Mimatsu-diagrams are still used and investigated at many volcano observatories worldwide (Poland et al., 2008; Wadge et al., 2009; Bretón-Gonzalez et al., 2013; Ratdomopurbo et al., 2013; Zobin et al., 2015). While these Mimatsu diagrams allow derivation of first-order parameters, such as investigating the general volume and outline of a dome, capturing the complete movement of the dome requires manual or automatic feature tracking techniques, as applied at lava flows (James et al., 2007) or at domes such as at Redoubt (Bull et al., 2013), Mt. St. Helens (Major et al., 2009; Walter, 2011), and Merapi (Walter et al., 2013b). Sophisticated tracking techniques often rely on mathematical correlation methods, such as the digital image correlation (DIC) or particle image velocimetry (PIV) techniques (Johnson et al., 2008; James et al., 2009; Walter et al., 2013a).

Our camera data were acquired by a 16 MPixel Nikon D5100 camera with an APS-C sensor and a resolution of 4928x3264 pixels. The camera is located at the Nevado de Colima (N19.564° W103.617°) at a distance of 5790 m from the centre of the Volcán de Colima summit (Figure 1). The camera is placed at a height of 3966 m above sea level, which is slightly higher than the summit height of Volcán de Colima at 3850 m. Due to the large distance between the camera and the target, we used a zoom lens with a focal length of 270 mm, ISO-100, equivalent to a 35-mm focal length of 405 mm. The camera was placed on a stable mount inside the observatory building. We use an external intervalometer for time-lapse control (Harbortronics Digisnap 2700); the batteries are solar powered, and the internal time is regularly synchronized by GPS. In the period January-April 2013, we set the camera to take one image every hour and recorded 2685 images (11 Nov. 2012 to 14 Mar. 2013); maximum night time exposure was limited to 2 seconds, to reduce battery power and storage consumption. Pixel brightness (from 0 to 255) allows a first-order image quality estimation. Daylight images and cloudy images have larger mean pixel brightness (from ~125 to 255) than night images (from 0 to 125). Furthermore, the cloudy and night images show a smaller contrast in pixel brightness (difference between minimum and maximum brightness), allowing us to identify clear daylight camera images (black dots in Figure 2) and cloud/night camera images (grey dots in Figure 2). The threshold value of the pixel brightness difference was arbitrarily defined as b=125 but was found to reduce the number of relevant images considerably (by 71%). From the remaining data we selected daily photos from similar daytimes, which could be used for digital image correlation analysis. The similar daytime image selection is of major benefit, since it minimizes the effect of shadowing and insulation changes on the image-to-image comparison.

To translate the pixel scale to metre scale, we used a high-resolution digital elevation model that is based on the combination of aerial photogrammetry and LiDAR data (Salzer et al., 2017). We found that the flat-topped 2007-11 dome summit was 162 m wide in the NE-SW direction (azimuth N50°), and its height was 45 m on the east side as measured to the crater trough. The field-of-view (FOV) was translated through geometric transformations to a metric FOV of 520 m x 344 m, and the pixel dimensions were accordingly approximated to 0.1 m x 0.1 m. The viewing direction was SSE, i.e., the westward lava flow formation was on the right side of the image. We assumed a constant pixel size, although pixels representing areas closer to the camera at the northern flank of the summit are certainly somewhat smaller. Because the camera distance to the summit is very large (5.79 km) and the dome dimension is very small (0.16 km), we assume that the constant pixel dimension is a reasonable simplification of the geometric problem (Figure 1).

Fixed installed time-lapse cameras have major advantages of stable viewing geometry and constant optical parameters. We observed, however, that the camera images show a systematic short-term and long-term shift associated with slight movements of the camera, probably due to outdoor temperature changes. For most scenarios, these slight movements are irrelevant. However, as we used a large 270 mm lens, the effect is clearly visible. Because our images were taken at the same time of day, this effect is reduced, and we further corrected the remaining shaking by simple image cross-correlation and shift translation.

We analysed the time-lapse data on a daily basis. First, we qualitatively describe any changes in morphology and degassing as observed in the images. Second, when growth of the dome occurred, we determine the displacement by applying the digital image correlation (DIC) technique, an image-matching method commonly used in computer vision studies. DIC permits the measurement of the shape, deformation and motion from two-dimensional array imaging data (Sutton et al., 2009). The idea is to first subdivide an image space into subregions and then compare the subregions by applying a correlation function. Using novel approaches of DIC, the accuracy of the subregion matching process can eventually result in position accuracies of 1/100 of a pixel (Schreier et al., 2000). More details on subregion conception, registration and the correlation procedure are provided in earlier reviews (Sutton et al., 2009). In our case, the impact due to variations in insulation isreduced by the selection of images from similar times of day. Our method is insensitive to variations in the intensity while being sensitive to the offset of intensity variations, where the shifted pixel pattern in the deformed image is estimated (Pan et al., 2009). The correlation criterion then allows the estimation of the degree of similarity between the subregions of the first (master) image and the second (deformed) image of the dome. More details of the so-called zero-normalized sum of the squared differences (ZNSSD) method, already applied for volcano data (Walter, 2011; Walter et al., 2013a), are given in (Pan et al., 2009). Subregion windows, with square dimensions, were selected in such a way that they were large enough to contain a distinctive intensity pattern but small enough to achieve a sub-pixel level of accuracy. In our case, the dimensions were 256x256 pixels during the first run and then incrementally decreasing to 64x64 pixels, with a constant subregion overlap of 75%. Decorrelation was defined to occur if less than three similar intensity peaks could be identified in a subset. Offsets on the order of 0.2 pixels could be detected, representing a displacement of 0.02 m for our camera. The main aim of the DIC analysis at Volcán de Colima is to trace the same physical subregions recorded in multiple images as a function of time. By applying this method we quantify the vertical and lateral growth of the dome and, for the first time, are able to identify the occurrence of gravitational spreading of a developing dome. The results are displayed in an image vector format for the selected area, and the full time series is shown for the central, western and eastern dome in binary plots. These results were then reproduced using numerical models in the discussion section.

# 3. Results

Seismic data indicate very clear precursors related to explosions 1 and 4 composed mainly of high-frequency events (Figure 2). The spectral amplitude increase can be related to these precursors preceding this pair of explosions. Explosions 2 and 3 were not preceded by such clear precursors. The seismic data are interpreted to show increasing rock fall activity starting at the end of February 2013.

## 3.1. Satellite radar

The satellite radar observations allowed an accurate depiction of the details at the summit region. Because of the consistent 11-day revisit interval, we obtain temporal information from this location. Slopes that face the satellite appear brighter and geometrically compressed, whereas slopes away from the satellite appear darker and geometrically stretched in the amplitude images. As shown in Figure 3, the slopes on the left side of the image, i.e., the western side in ascending images, appear brighter. Images acquired on earlier dates are available but do not show any visible difference in amplitudes.

The image acquired 3 hours before the 6 January explosion displays the flat-topped 2007-11 dome situated off-centre in a larger crater area within the older 2005 crater with a much larger diameter (Figure 3). The flat-topped dome displays small-scaled shadow regions associated with small depressions at the surface. The next image acquired on 17 January displays a very pronounced nested crater, with a younger circular crater formed within the 2007-2011 lava dome. In the centre of the latter crater, we identify a structure that is bright on its left side and dark on its right side (Figure 3b). As the satellite is looking from the left (ascending images), the central structure of this crater is a locally elevated region. Due to the near circular structure of the elevated region, TSX data allow the interpretation of new dome growth during this early stage, which is in agreement with overflight observations (on 14 January). The following images acquired on 28 January show a general decrease in amplitude contrast at the dome, interpreted as the accumulation of ash material in this region (Figure 3c). Amplitude ratio maps illustrate the extent of the nested crater structure and the presence of the new dome that is imminent inside the newly developed crater (Figure 3d).

Another major crater deepening is observed another 11 days later on 8 February 2013, followed again by new dome growth on 19 February that widens in dimension and starts overflowing the crater rim in the TSX images on 2 March 2013 (Figures 3e-h). Amplitude ratio maps clearly depict the dimension and lateral growth of the dome, dominantly increasing to the west and east. The following images of the TSX amplitude merely show continued spreading of the dome (Figures 3i-l), which overflowed the west side, and on the east side, the dome started to fill the entire crater that developed in the first week of the new eruption phase.

**3.2. Time-lapse camera**

The camera images are of very high resolution and allow the identification of structures at an unprecedented level of detail. Here, we also present images acquired by the time-lapse camera before the eruption during an alleged period of dormancy of the volcano. The old 2007-2011 dome of Volcán de Colima is clearly depicted by the flat silhouette in the 9 December 2012 daily images. In addition, we observed only minor degassing located on the western rim of the dome, as indicated in Figure 4. On 3 January 2013, just three days before the eruption, the summit region was snow covered. On 5 January, snow coverage is still visible, and the appearance of new fumaroles is seen on the western dome summit (Figure 4d). These fumaroles appear elongated and clearly develop and eventually connect to become a ring-like structure on 6 January, clearly visible in time-lapse camera images just 2-3 hours prior to the eruption (Figures 4e-f). The first visible image taken after the initial explosion on 6 January (Figure 4g) shows (now snow free) the presence of a steep-walled crater located on the western part of the dome. In fact, the location of this crater (crater-1 in Figure 4g) resembles the location of the previous fumaroles, as the crater rim almost exactly follows the ring-shaped gas emission outline identified before the explosion.

Due to limited visibility, the next clear images were not available until 10 January 2013 (Figure 5a), followed by an explosion carving a pronounced crater located more to the east on the flat summit region of the dome (Figures 5b-c). This crater-2 was not preceded by visible fumarole activity but was followed by fumarolic emission mainly on its eastern rim (left side in Figure 5d). The outline of crater-2 partly follows the outline of crater-1 but also widens the eastern extent, while the western crater region was covered by tephra. At the location of the strongest fumarole activity on 13 January (Figure 5d), another explosion occurred afterwards on the same day, leaving a small crater (crater-3) within the eastern sector. The following images generally show intensifying fumarole activity, but distinct new crater formations cannot be identified in the camera images throughout the rest of January 2013. However, we identify the presence of a noticeable block in the 29 January image that was not observed before. The dimensions are estimated to be 9x21 m, and assuming a rotational ellipsoidal shape, this block had a volume of over 7000 $m^2$. Close inspection of the high resolution camera images reveals that the block has a flat surface, rounded edges and that shows few open fractures. Assuming this was deposited as a bomb it was transported approximately 80-100 m away from the main crater centre. Assuming a 100 m flight distance and a 50 m flight height, we project the bomb was ejected at 63 degrees at a velocity of over 35 m/s. No further evidence of an explosion was observed, in agreement with the seismic records (Figure 2).

The next clear time-lapse images showing changes were recorded on 14 February 2013, where the first tip of the dome becomes visible. We note that the TSX data indicated the first appearance of a first dome building phase on 17 January, but the main dome building phase occurred on 19 February. The camera data here add details on the horizontal and vertical growth above the crater rim. The new dome grew vertically on 21 and 26 February (Figures 6b-c). After 21 February, the dome appeared to mainly grow laterally to the west and east (Figures 6c, d, e). On 3 March, the dome started overflowing the western crater rim and commenced the formation of a lava flow (Figure 6f). From that moment, we observe repeated oversteepening and lateral flow directed westward.

### 3.3. Image correlation

Tracking distinct features in the image dataset means that quantitative information on this dome growth episode can be generated, as seen in the time-lapse camera images (Figure 7). The DIC method allows the tracking of features in the image domain that do not change their optical properties but move by geometric rotation and translation (Walter, 2011). Applied to the dome, we observe first upwardly directed growth (Figure 7a), which is slightly directed westward at its summit on 18 February 2013. This growth is followed by small local subsidence, such as on 23 February, after which the growth resumes again and is clearly identified on 24 February (Figure 7c) directed radially away from the centre of extrusion. A few days later, we again see minor subsidence of the dome and lateral spreading of both the eastern and western flanks. After a short growth pulse to the east, the dome commences to mainly grow westwards, associated with the overflow over the western crater rim (Figure 7f). The vertical growth of the dome is minor, if detected at all at this stage.

By depicting subregions of 100x100 pixels (or 10x10 m) in the centre and on the western and eastern flanks of the newly developed dome, we can generate time-growth graphs, as represented in Figure 8. The height of the dome is first seen to grow almost linearly, and then, as a critical dome height is reached, we observe a pronounced trend change (on 20 February). From that moment, vertical growth is much slower. As vertical growth decreases, we identify an increase in lateral growth, which is more strongly expressed on the western dome flank than on the eastern flank. This asymmetry evolves, producing overflow of the western crater rim.

Comparing the available datasets we calculate the half dome volume changes, dividing the dome into western and eastern sections. The volumetric changes are provided in Figure 8, showing that the western dome section first grew slowly in volume. Then it showed a sudden increase when the first crater overflow occurred on 2-3 March, followed by a short decrease before a sharp increase to $3.2x10^5$ m³ was observed. The growth of the eastern dome in turn became stable, with a near linear volume increase, reaching $1.2x10^5$ m³ after the same period. Therefore, our results indicate that crater rim overflow was associated with an increase in the eruption rate, directed on the western side, whereas the eastern half of the dome was not affected.

# 4. Discussion

A large number of volcanoes worldwide host lava domes, and since they represent a major source of hazards, understanding their growth patterns from vertical to lateral growth and eventual crater overflow is important. Lava domes commonly grow in summit regions or craters of volcanoes, and details of their initial formation can be studied by joint satellite radar and time-lapse camera monitoring as discussed below.

### 4.1. Advantages and limitations of the combined satellite and camera observations

Previous studies on lava dome growth have used satellite radar observations (Salzer et al., 2014; Salzer et al., 2017) or camera time-lapse observations (Walter et al., 2013a), but a combined analysis of these two data sets has not yet been pursued. Here we demonstrated that by using satellite radar data and terrestrial camera data, the interpretation and identification of crater and lava-dome activities might be significantly improved. This has two main reasons, first the different viewing perspectives, and second the different resolution.

The viewing perspective of the satellite radar allows analysis of the crater and dome geometry in near plain view. Amplitude differences resulting from geometric changes allow to identify crater formation and early development of a lava dome inside this crater. The regular acquisition mode every 11 days is independent on sunshine and delivers clear views even through eruption clouds. For instance, due to poor visibility on 17 January the radar observations were the only way of observing the crater and dome. The viewing perspective of the camera, in turn, allows analysis of the growth in the field of view, and measurement of dome height and its west-east growth. As the camera was located on similar elevation, this viewing geometry inhibited a closer view into the crater, so that only those domes could be assessed that grow vertically above the crater rim. Therefore first dome was observed in the cameras one month after it was first identified in satellite radar. Therefore, the time-lapse cameras we used, although configured in high resolution and located at a similar elevation to the volcano summit, did not capture the full details of dome growth. The first small dome that grew during 14-17 January was completely hidden from the camera, since it was growing inside the newly formed crater.

The second phase of dome growth became visible from 8-19 February once it appeared above the crater rim.

A major advantage of the camera is that also sites of steaming could be investigated, and a clear geometric association to later crater forming eruptions be described. No such steaming could be identified in radar data.

Resolution of both sensors was very high, the radar data had a spot mode acquisition plan providing meter-scale resolution, whereas the cameras even allow centimeter-scale resolution. This 16 MPixel camera resolution was strongly needed for identifying details of the steaming, the crater shapes, and the growth and spreading of the dome. Temporal resolution that is the time distance between two satellite passes or two images taken was strongly different. The TerraSAR-X satellite acquires every 11 days, the camera was set up to 1 image per hour. New camera installations realized by the GFZ and the University of Colima after 2015 now even allow online adjustment of the frame rate and resolution.

From the high spatial and temporal resolution of time-lapse camera observations we could apply an image correlation technique to observe dome growth prior to crater overflow. Our records indicate initial linear vertical dome growth, until the crater was refilled by fresh dome material and rim overflow commenced. This overflow changed the dynamics of the dome growth episode, as our image correlation results revealed. A major influence of the pre-existing crater morphology on dome dynamics could not be observed, but we found that the overflow occurrence concurs with a growth rate change on the western part of the dome. We also tested pixel offset calculation results in the satellite radar observations, however as the ground is rapidly changing over an 11-day TerraSAR-X repeat cycle, the subregion window correlation approach was not found to yield stable results for the available radar data.

Future studies could potentially more quantitatively fuse and combine satellite and camera time-lapse observation, especially for slow changes occurring at lava-domes of

Volcán de Colima. In this study the consideration of both dataset was relevant for developing a chronology of events (Figure 10).

To obtain a view of the deep summit craters, we found that dome growth initiation, with dimensions of 10 m or even less, can be well identified in high resolution (spot mode) satellite radar images. Moreover, by use of time-lapse cameras ideally operating from different sides, our displacement monitoring approach can theoretically be automatized. Also at other dome-building volcanoes, such as Merapi (Indonesia), Mount St. Helens (USA), Bezymianny (Russia), time-lapse cameras have been installed for routine monitoring, now allowing quantitative analysis of lava-dome volumes, height change measurements and spreading assessment prior to dome instability. As an alternative, future studies may consider low cost unmanned aerial devices, to collect aerial photos from a safe distance and from different viewing perspectives.

**4.2. Ring-shaped emission pattern and explosion craters**

The excavation of craters at the summit of Volcán de Colima was interpreted to be associated with four Vulcanian explosions (between 6 and 29 January), with effusive activity occurring during some of this period (Zobin et al., 2015). These early Vulcanian explosions excavated a number of craters, partially overlapping (nested), that we could clearly identify in satellite radar and time-lapse camera images. Precursory inflation was observed by an InSAR study by combining TerraSAR-X acquisitions from 26 December 2012 and 6 January 2013 (Salzer et al., 2014). Seismicity preceded the first explosion by 2 days (Arámbula-Mendoza et al., 2018) and was also well identified prior to explosion 4 by high-frequency events. Explosions 2 and 3, in turn, were not preceded by similar precursors. The presence and migration of fumarole sites prior to eruptions as recorded by our time-lapse cameras is of particular interest. Our data show weak degassing prior to some explosions (explosions 1, 3 and 4), which might be interpreted as precursory activity as well. The strongest degassing precursor was found prior to explosions 1 and

4, which is in agreement with the high frequency seismicity identified prior to the explosion.

The relevance of the snowfall prior to the first explosion is still unclear. Snowfall in early January is not uncommon, but might have notably contributed to the expression of gas emission visible in the cameras. Snow at fumaroles is melting first, and increase of the visible steaming effect following such precipitation events, associated with infiltration of water into the ground and cooling of high temperature fumaroles is documented elsewhere (Zimmer et al., 2017).

The four Vulcanian explosions (on 6, 11, 13 and 29 January) reached up to 2500 m in height and caused minor pyroclastic flows travelling westward. Associated with these explosions, we show the location and expression of at least three well-identified nested craters. The cameras could not identify further excavation of the cratered structure associated with explosion 4, but this explosion left a bomb of considerable size on the NE margin of the 2007-2011 old dome.

This study underlines that improving the resolution of time lapse photographs enables better observation of surface degassing and crater dynamics, which in turn may allow identification of precursors associated with Vulcanian eruptions. While a previous study with lower resolution photos could not identify fumarole emission (Zobin et al., 2015), our higher resolution photos reveal their presence and even show details of a correlation with structure. Specifically, minor fumarole emission was first identified one day prior to the first explosion on the western margin, and it was then observed to propagate along a semicircular perimeter on the upper edge of the 2007-2011 dome. The 6 January explosion crater had a perimeter size that almost perfectly agrees with the precursory ring-shaped gas emission zone. Ring-shaped precursory expressions of gas emissions have been observed at dome-building volcanoes elsewhere, commonly during the first stages of an explosion, which are associated with a pulse of magma extrusion (Johnson et al., 2008). Assuming that a similar degassing mechanism is responsible as proposed for the Santiaguito dome complex, the ring-shaped emission pattern would be geometrically associated with shearing at the conduit margins (Bluth and Rose, 2004), and/or degassing may display a short-term and shallow dislocation event directly associated with magma arrival (Johnson et al., 2008). Of interest here is that the ring-shaped emission pattern is observed days before the actual eruption and not just seconds or minutes prior to it. In some cases, only partial degassing rings are found, such as prior to the fourth explosion at Volcán de Colima on 29 January. Given that the ring-shaped emission pattern is temporally associated with an increase in seismicity (Figure 2), it may also explain the two-phase seismic signals (Zobin et al., 2015). Before the co-explosive high-frequency phase occurred, a low-frequency signal was identified as a precursory phase. These signals may be associated with magma and fluid rise manifesting in the ring-shaped emission pattern we identified. A general degassing increase prior to eruptions was also observed for other eruptions at Volcán de Colima, but this paper is the first to describe the ring-shaped nature in detail.

### 4.3. Critical dome height and gravitational spreading

We investigate the dome growth scenario as quantified by camera data. For the modelling we use the two-dimensional discrete element method (DEM) software PFC2D (Itasca Consulting Group, 2017) and follow the method outlined by Harnett et al. (2018). This DEM software creates material out of rigid particles that interact with neighbouring particles via elastic contact laws, where particles carry a force and moment that are updated per model time step. We incorporate different bond styles to model both fluid behaviour for the lava dome core (parallel bonds, (Potyondy and Cundall, 2004)) and solid behaviour in the outer carapace and talus regions (flat jointed bonds, (Potyondy, 2012)).

The model is initialized with a "batch" of magma in the conduit, whereby magma viscosity is determined by the bond stiffness of this material (Husain et al., 2014). We use a viscosity of $10^9$ Pa.s, following estimates of apparent magma viscosity at Volcán de Colima in the range $10^9$ to $10^{11}$ (Lavallee et al., 2007; Lavallee et al., 2008; Kendrick et al., 2012). Constant extrusion is then simulated by adding an upward velocity to material in the conduit, and solidification is tracked throughout the model run. A more viscous dome is likely to be taller and less prone to lateral spreading, whereas a less viscous dome would likely not reach the heights seen from observational data. Similar to previous lava dome emplacement models (Hale and Wadge, 2008; Hale et al., 2009a; Hale et al., 2009b; Husain et al., 2014), we use the solidus pressure to model the lava solidification process and therefore track the boundary between the fluid core and solid carapace. The mechanical properties of the dome rock are hard to determine at a rock mass scale, despite previous studies on Volcán de Colima andesites at a laboratory scale (Heap et al., 2014; Heap et al., 2016). We therefore use the morphology of the growing dome to estimate mechanical rock strength by using a calibration procedure process in PFC (e.g., (Holt et al., 2005; Holohan et al., 2011; Holohan et al., 2017) and matching the model morphology to the observed morphology (Figure 9). This estimation was achieved through a forward modelling approach (Harnett et al., 2018), and the model results were corrected to account for the 2-dimensional nature of the model (see Appendix).

Matching the model morphology to the observed dome morphology, a peak rock strength of ~3.7 MPa is necessary to yield a critical dome height at which vertical growth abruptly decreases, as observed by the camera data. This strength value is ~20% of the lowest laboratory values and suggests an intense level of fracturing and/or porosity that is present in a cooling and dynamically evolving carapace that has a significant effect on the rock behaviour at a rock mass scale (Zorn et al., 2018). To match the observed dome growth, a reduction in Young's modulus is required from 8.1 GPa in the tested dome rock from Volcán de Colima to 3.5 GPa. This reduction alludes not only to the importance of fracturing, but also the importance of scaling both the strength and elastic parameters of material from the laboratory sample scale to a rock mass scale (Heap et al., 2018).

The modelled dome growth shown in Figure 9 shows a morphology similar to the observed dome growth at Volcán de Colima during February/March 2013. Early dome growth is dominated by vertical growth and an initial increase in height; the explicit width of this growth in the early stage of the model is determined by the initial conditions imposed for the width of the conduit (Figure 9). A height threshold is reached, after which horizontal growth exerts greater control over the lava dome growth (critical height). This means that initially, the dome extrudes and solidifies very quickly so creates a near-vertical spine. Once sufficient dome material is extruded, the dome is able to maintain ductile core material within it (and therefore transitions to a more endogenous-style growth). This horizontal growth increase is accordingly interpreted to be due to increased gravitational spreading of the rock mass. As observed in the camera image analysis, oversteepening occurs on the dome flanks, along with the generation of rubbly spine-type features towards the apex of the dome. Although the steep vertical growth observed initially at Volcán de Colima is reproduced well, small differences may suggest an initially stronger material. Possibly, the first magma extrusion could be more degassed and, hence, more viscous; the initial vertical growth domain is therefore likely associated with extrusion of a viscous plug and conduit material before fresh magma reached the surface and spread laterally. Future studies may also be needed to understand the effect of temperature on rock strength.

We note that the models are 2D only and that matching the exact timing of the dome growth phases is challenging, as complete temporal coverage of the extrusion process is not available. The modelled dome starts extruding at time zero, and comparisons are made to the monitored dome until it starts to overflow the crater rim. This model gives a fixed frame of reference and allows comparison against normalized time relative to the dome width. The compared time series of the modelled and observed dome growth can therefore be relatively shifted in the time domain by several days.

# 5. Conclusions

At Volcán de Colima, new excavations of several nested summit craters were observed in detail by high-resolution satellite radar data and by a time-lapse monitoring camera. We could identify crater excavation associated with three Vulcanian explosions in January 2013 and deposition of a major bomb outside of the crater. The craters were carved into the cooled 2007-2011 dome material, with variations observed in the crater geometry and position during successive Vulcanian explosions. Prior to the crater formation, pronounced degassing was observed, partially with a ring-shaped emission pattern, identifying the location of the later explosion crater excavation. Following this destructive crater-forming activity at Volcán de Colima, an early dome formation episode was observed. While the high-resolution TerraSAR-X spotmode satellite radar images allow imaging the early dome deep inside the excavated craters, the permanently installed monitoring cameras allow tracing the details of dome growth once the dome reached the height of the crater rim. Using PIV, we perform an image-to-image comparison and optical flow field, allowing the identification of initial vertical dome growth. This vertical growth gradually changed to lateral growth caused by gravitational spreading of the dome material. The dome continued to grow laterally, and to a minor degree also vertically, until it overflowed the margin of the crater and developed into a lava flow. We compare these dome growth observations to discrete element models, and find that the observed dome morphology can be matched if the lava dome peak rock strength is significantly lower than common laboratory values.

**Acknowledgements**

This is a contribution to VOLCAPSE, a research project funded by the European Research Council under the European Union's H2020 Programme / ERC consolidator grant n. [ERC-CoG 646858]. The TerraSAR-X images were provided by the German Aerospace Center (DLR proposal ID 1505). CH acknowledges funding from a NERC DTP place (grant number NE/L002564/1) and a place on the Itasca Educational Partnership, with thanks to Matt Purvance. The authors thank Mike Heap for the provision of laboratory data from Volcán de Colima. The authors wish to thank Jose Manuel Alvarez Nieves for technical assistance and company in the field at Volcán de Colima.

## References

Abrams, M., Glaze, L. and Sheridan, M., 1991. Monitoring Colima Volcano, Mexico, Using Satellite Data. Bulletin of Volcanology, 53(7), 571-574.

Adams, R.J., Perger, W.F., Rose, W.I. and Kostinski, A., 1996. Measurements of the complex dielectric constant of volcanic ash from 4 to 19 GHz. J Geophys Res-Sol Ea, 101(B4), 8175-8185.

Arámbula-Mendoza, R., Reyes-Dávila, G., Vargas-Bracamontes, D.M., González-Amezcua, M., Navarro-Ochoa, C., Martínez-Fierros, A. and Ramírez-Vázquez, A., 2018. Seismic monitoring of effusive-explosive activity and large lava dome collapses during 2013-2015 at Volcan de Colima, Mexico. Journal of Volcanology and Geothermal Research, 351, 75-88.

Arnold, D.W.D., Biggs, J., Wadge, G. and Mothes, P., 2018. Using satellite radar amplitude imaging for monitoring syn-eruptive changes in surface morphology at an ice-capped stratovolcano. Remote Sensing of Environment, 209, 480-488.

Belousov, A., Belousova, M. and Voight, B., 1999. Multiple edifice failures, debris avalanches and associated eruptions in the Holocene history of Shiveluch volcano, Kamchatka, Russia. Bulletin of Volcanology, 61(5), 324-342.

Bluth, G.J.S. and Rose, W.I., 2004. Observations of eruptive activity at Santiaguito volcano, Guatemala. Journal of Volcanology and Geothermal Research, 136(3-4), 297-302.

Bretón-Gonzalez, M., Campos, A., León, Z., Plascencia, I. and Ramírez, J.J., 2013. The 2007–2012 lava dome growth in the crater ofVolcán de Colima, México, derived from Video Monitoring System. In: V.M. Zobin (Editor), Complex monitoring of volcanic activity: methods and results. Nova Science Publishers Inc., Hauppage, pp. 153–169.

Bull, K.F., Anderson, S.W., Diefenbach, A.K., Wessels, R.L. and Henton, S.M., 2013. Emplacement of the final lava dome of the 2009 eruption of Redoubt Volcano, Alaska. Journal of Volcanology and Geothermal Research, 259, 334-348.

Carr, B.B., Clarke, A.B. and Vanderkluysen, L., 2016. The 2006 lava dome eruption of Merapi Volcano (Indonesia): Detailed analysis using MODIS TIR. Journal of Volcanology and Geothermal Research, 311, 60-71.

Cashman, K.V., Pallister, J.S., Thornber, C.R. and Anonymous, 2006. Extreme decompression-induced crystallization during the 2004-present eruption of Mount St. Helens; implications for shallow deformation mechanisms.

Castro, J.M., Cordonnier, B., Tuffen, H., Tobin, M.J., Puskar, L., Martin, M.C. and Bechtel, H.A., 2012. The role of melt-fracture degassing in defusing explosive rhyolite eruptions at volcan Chaiten. Earth and Planetary Science Letters, 333, 63-69.

Chaussard, E., 2017. A low-cost method applicable worldwide for remotely mapping lava dome growth. Journal of Volcanology and Geothermal Research, 341, 33-41.

Christiansen, R.L. and Peterson, D.W., 1981. The 1980 eruptions of Mount St. Helens, Washington. Chronology of the 1980 eruptive activity. U.S. Geological Survey Professional Paper, 1250, 17-30.

Cortes, A., Macias, J.L., Capra, L. and Garduno-Monroy, V.H., 2010. Sector collapse of the SW flank of Volcan de Colima, Mexico The 3600 yr BP La Lumbre-Los Ganchos debris avalanche and associated debris flows. Journal of Volcanology and Geothermal Research, 197(1-4), 52-66.

Dalfsen, E.D., Richter, N., Gonzalez, G. and Walter, T.R., 2017. Geomorphology and structural development of the nested summit crater of Lascar Volcano studied with Terrestrial Laser Scanner data and analogue modelling. Journal of Volcanology and Geothermal Research, 329, 1-12.

Darmawan, H., Walter, T.R., Brotopuspito, K.S., Subandriyo and Nandaka, I.G.M.A., 2018. Morphological and structural changes at the Merapi lava dome monitored in 2012-15 using unmanned aerial vehicles (UAVs). Journal of Volcanology and Geothermal Research, 349, 256-267.

Diefenbach, A.K., Crider, J.G., Schilling, S.P. and Dzurisin, D., 2012. Rapid, low-cost photogrammetry to monitor volcanic eruptions: an example from Mount St. Helens, Washington, USA. Bulletin of Volcanology, 74(2), 579-587.

Fink, J.H. and Anderson, S.W., 2000. Lava domes and Coulees. Academic Press, San Diego, 307-319 pp.

Fink, J.H. and Griffiths, R.W., 1998. Morphology, eruption rates, and rheology of lava domes: Insights from laboratory models. J Geophys Res-Sol Ea, 103(B1), 527-545.

Hale, A.J., Calder, E.S., Loughlin, S.C., Wadge, G. and Ryan, G.A., 2009a. Modelling the lava dome extruded at Soufriere Hills Volcano, Montserrat, August 2005-May 2006 Part II: Rockfall activity and talus deformation. Journal of Volcanology and Geothermal Research, 187(1-2), 69-84.

Hale, A.J., Calder, E.S., Wadge, G., Loughlin, S.C. and Ryan, G.A., 2009b. Modelling the lava dome extruded at Soufriere Hills Volcano, Montserrat, August 2005-May 2006 Part I: Dome shape and internal structure. Journal of Volcanology and Geothermal Research, 187(1-2), 53-68.

Hale, A.J. and Wadge, G., 2008. The transition from endogenous to exogenous growth of lava domes with the development of shear bands. Journal of Volcanology and Geothermal Research, 171(3-4), 237-257.

Harnett, C.E., Thomas, M.E., Purvance, M.D. and Neuberg, J., 2018. Using a discrete element approach to model lava dome emplacement and collapse. Journal of Volcanology and Geothermal Research.

Heap, M.J., Lavallee, Y., Petrakova, L., Baud, P., Reuschle, T., Varley, N.R. and Dingwell, D.B., 2014. Microstructural controls on the physical and mechanical properties of edifice-forming andesites at Volcan de Colima, Mexico. J Geophys Res-Sol Ea, 119(4), 2925-2963.

Heap, M.J., Russell, J.K. and Kennedy, L.A., 2016. Mechanical behaviour of dacite from Mount St. Helens (USA): A link between porosity and lava dome extrusion mechanism (dome or spine)? Journal of Volcanology and Geothermal Research, 328, 159-177.

Heap, M.J., Villeneuve, M., Farquharson, J.I., Albino, F., Brothelande, E., Amelung, F. and Got, J.L., 2018. Towards more realistic values of elastic moduli for volcano modelling, GU General Assembly Vienna Geophysical Research Abstracts, Vienna, pp. EGU2018-3909.
Holohan, E.P., Schopfer, M.P.J. and Walsh, J.J., 2011. Mechanical and geometric controls on the structural evolution of pit crater and caldera subsidence. J Geophys Res-Sol Ea, 116.
Holohan, E.P., Sudhaus, H., Walter, T.R., Schopfer, M.P.J. and Walsh, J.J., 2017. Effects of Host-rock Fracturing on Elastic-deformation Source Models of Volcano Deflation. Sci Rep-Uk, 7.
Holt, R.M., Kjolaas, J., Larsen, I., Li, L., Pillitteri, A.G. and Sonstebo, E.F., 2005. Comparison between controlled laboratory experiments and discrete particle simulations of the mechanical behaviour of rock. Int J Rock Mech Min, 42(7-8), 985-995.
Hooper, D.M. and Mattioli, G.S., 2001. Kinematic modeling of pyroclastic flows produced by gravitational dome collapse at Soufriere Hills volcano, Monstserrat. Natural Hazards, 23(1), 65-86.
Huppert, H.E., Shepherd, J.B., Sigurdsson, R.H. and Sparks, S., 1982. On lava dome growth, with application to the 1979 lava extrusion of the Soufriere of St. Vincent. Journal of Volcanology and Geothermal Research, 14(3-4), 199-222.
Husain, T., Elsworth, D., Voight, B., Mattioli, G. and Jansma, P., 2014. Influence of extrusion rate and magma rheology on the growth of lava domes: Insights from particle-dynamics modeling. Journal of Volcanology and Geothermal Research, 285, 100-117.
Itasca Consulting Group, I., 2017. PFC2D (Particle Flow Code in Two Dimensions).
James, M.R., Pinkerton, H. and Applegarth, L.J., 2009. Detecting the development of active lava flow fields with a very-long-range terrestrial laser scanner and thermal imagery. Geophysical Research Letters, 36.
James, M.R., Pinkerton, H. and Robson, S., 2007. Image-based measurement of flux variation in distal regions of active lava flows. Geochemistry Geophysics Geosystems, 8, Q03006.
James, M.R. and Varley, N., 2012. Identification of structural controls in an active lava dome with high resolution DEMs: Volcán de Colima, Mexico. Geophys. Res. Lett., 39(22), L22303.
Johnson, J.B., Lees, J.M., Gerst, A., Sahagian, D. and Varley, N., 2008. Long-period earthquakes and co-eruptive dome inflation seen with particle image velocimetry. Nature (London), 456(7220), 377-381.
Kendrick, J.E., Lavallee, Y., Ferk, A., Perugini, D., Leonhardt, R. and Dingwell, D.B., 2012. Extreme frictional processes in the volcanic conduit of Mount St. Helens (USA) during the 2004-2008 eruption. Journal of Structural Geology, 38, 61-76.
Lamb, O.D., De Angelis, S., Wall, R.J., Lamur, A., Varley, N.R., Reyes-Davila, G., Arambula-Mendoza, R., Hornby, A.J., Kendrick, J.E. and Lavallee, Y., 2017. Seismic and experimental insights into eruption precursors at Volcan de Colima. Geophys Res Lett, 44(12), 6092-6100.
Lavallee, Y., Hess, K.U., Cordonnier, B. and Dingwell, D.B., 2007. Non-Newtonian rheological law for highly crystalline dome lavas. Geology, 35(9), 843-846.
Lavallee, Y., Meredith, P.G., Dingwell, D.B., Hess, K.U., Wassermann, J., Cordonnier, B., Gerik, A. and Kruhl, J.H., 2008. Seismogenic lavas and explosive eruption forecasting. Nature (London), 453(7194), 507-510.
Lavallee, Y., Varley, N.R., Alatorre-Ibarguengoitia, M.A., Hess, K.U., Kueppers, U., Mueller, S., Richard, D., Scheu, B., Spieler, O. and Dingwell, D.B., 2012. Magmatic architecture of dome-building eruptions at Volcan de Colima, Mexico. Bulletin of Volcanology, 74(1), 249-260.
Luhr, J., 1981. Colima; history and cyclicity of eruptions. Volcano News(7), 1-3.

Luhr, J. and Prestegaard, K., 1985. Caldera formation at Volcan Colima, Mexico; a large, Mount St. Helen-type avalanche event 4,300 years ago. Eos, Transactions, American Geophysical Union, 66(18), 411.

Major, J.J., Dzurisin, D., Schilling, S.P. and Poland, M.P., 2009. Monitoring lava-dome growth during the 2004-2008 Mount St. Helens, Washington, eruption using oblique terrestrial photography. Earth and Planetary Science Letters, 286(1-2), 243-254.

Major, J.J., Kingsbury, C.G., Poland, M.P. and LaHusen, R.G., 2008. Extrusion rate of the Mount St. Helens lava dome estimated from terrestrial imagery, November 2004-December 2005. U. S. Geological Survey Professional Paper, 1750, 237-255.

Major, J.J., Poland, M.P., Kingsbury, C.G., Dzurisin, D., LaHusen, R.G. and Anonymous, 2005. Quantifying spatial and temporal variance in apparent growth rate of the 2004-05 Mount St. Helens lava dome from single-camera images. Abstracts with Programs - Geological Society of America, 37(7), 531.

Mimatsu, M., 1995. Showa-Shinzan Diary, Sobetsu Town Office, Usu, Hokkaido.

Minakami, T., Ishikawa, T. and Yagi, K., 1951. The 1944 eruption of volcano Usu in Hokkaido, Japan. Bulletin of Volcanology, 11, 45–157.

Miyamachi, H., Watanabe, H., Moriya, T. and Okada, H., 1987. Seismic experiments on Showa-Shinzan lava dome using firework shots. pure and applied geophysics, 125(6), 1025-1037.

Mueller, S.B., Varley, N.R., Kueppers, U., Lesage, P., Davila, G.A.R. and Dingwell, D.B., 2013. Quantification of magma ascent rate through rockfall monitoring at the growing/collapsing lava dome of Volcan de Colima, Mexico. Solid Earth, 4(2), 201-213.

Newhall, C.G. and Melson, W.G., 1983. Explosive activity associated with the growth of volcanic domes. Journal of Volcanology and Geothermal Research, 17(1-4), 111-131.

Nishiyama, R., Miyamoto, S., Okubo, S., Oshima, H. and Maekawa, T., 2017. 3D Density Modeling with Gravity and Muon-Radiographic Observations in Showa-Shinzan Lava Dome, Usu, Japan. Pure and Applied Geophysics, 174(3), 1061-1070.

Ogburn, S.E., Loughlin, S.C. and Calder, E.S., 2015. The association of lava dome growth with major explosive activity (VEI >= 4): DomeHaz, a global dataset. Bulletin of Volcanology, 77(5).

Pallister, J.S., Schneider, D.J., Griswold, J.P., Keeler, R.H., Burton, W.C., Noyles, C., Newhall, C.G. and Ratdomopurbo, A., 2013. Merapi 2010 eruption-Chronology and extrusion rates monitored with satellite radar and used in eruption forecasting. Journal of Volcanology and Geothermal Research, 261, 144-152.

Pan, B., Qian, K., Xie, H. and Asundi, A., 2009. Two-dimensional digital image correlation for in-plane displacement and strain measurement: a review. Measurement Science and Technology, 20(062001), 1-17.

Pinel, V., Hooper, A., de la Cruz-Reyna, S., Reyes-Davila, G., Doin, M.P. and Bascou, P., 2011. The challenging retrieval of the displacement field from InSAR data for andesitic stratovolcanoes; case study of Popocatepetl and Colima Volcano, Mexico. Journal of Volcanology and Geothermal Research, 200(1-2), 49-61.

Poland, M.P., Dzurisin, D., LaHusen, R.G., Major, J.J., Lapcewich, D., Endo, E.T., Gooding, D.J., Schilling, S.P. and Janda, C.G., 2008. Remote camera observations of lava dome growth at Mount St. Helens, Washington, October 2004 to February 2006. U S Geological Survey Professional Paper, Report: P 1750, 225-236.

Portal, A., Gailler, L.S., Labazuy, P. and Lenat, J.F., 2016. Geophysical imaging of the inner structure of a lava dome and its environment through gravimetry and magnetism. Journal of Volcanology and Geothermal Research, 320, 88-99.

Potyondy, D.O., 2012. A flat-jointed bonded-particle material for hard rock, 46th US Rock Mech. Symp. .

Potyondy, D.O. and Cundall, P.A., 2004. A bonded-particle model for rock. Int J Rock Mech Min, 41(8), 1329-1364.

Ratdomopurbo, A., Beauducel, F., Subandriyo, J., Nandaka, I.G.M.A., Newhall, C.G., Suharna, Sayudi, D.S., Suparwaka, H. and Sunarta, 2013. Overview of the 2006 eruption of Mt. Merapi. Journal of Volcanology and Geothermal Research, 261, 87-97.

Reyes-Davila, G.A., Arambula-Mendoza, R., Espinasa-Perena, R., Pankhurst, M.J., Navarro-Ochoa, C., Savov, I., Vargas-Bracamontes, D.M., Cortes-Cortes, A., Gutierrez-Martinez, C., Valdes-Gonzalez, C., Dominguez-Reyes, T., Gonzalez-Amezcua, M., Martinez-Fierros, A., Ramirez-Vazquez, C.A., Cardenas-Gonzalez, L., Castaneda-Bastida, E., de los Monteros, D.M.V.E., Nieto-Torres, A., Campion, R., Courtois, L. and Lee, P.D., 2016. Volcan de Colima dome collapse of July, 2015 and associated pyroclastic density currents. Journal of Volcanology and Geothermal Research, 320, 100-106.

Salzer, J.T., Milillo, P., Varley, N., Perissin, D., Pantaleo, M. and Walter, T.R., 2017. Evaluating links between deformation, topography and surface temperature at volcanic domes: Results from a multi-sensor study at Volcan de Colima, Mexico. Earth and Planetary Science Letters, 479, 354-365.

Salzer, J.T., Nikkhoo, M., Walter, T.R., Sudhaus, H., Reyes-Dávila, G., Bretón, M. and Arámbula, R., 2014. Satellite radar data reveal short-term pre-explosive displacements and a complex conduit system at Volcán de Colima, Mexico. Frontiers in Earth Science, 2(12).

Saucedo, R., Macias, J.L., Gavilanes, J.C., Arce, J.L., Komorowski, J.C., Gardner, J.E. and Valdez-Moreno, G., 2010. Eyewitness, stratigraphy, chemistry, and eruptive dynamics of the 1913 plinian eruption of Volcan de Colima, Mexico. Journal of Volcanology and Geothermal Research, 191(3-4), 149-166.

Schreier, H.W., Braasch, J.R. and Sutton, M.A., 2000. On Systematic Errors in Digital Image Correlation. Optical Engineering, 39(11), 2915–2921.

Sheldrake, T.E., Sparks, R.S.J., Cashman, K.V., Wadge, G. and Aspinall, W.P., 2016. Similarities and differences in the historical records of lava dome-building volcanoes: Implications for understanding magmatic processes and eruption forecasting. Earth-Sci Rev, 160, 240-263.

Stevenson, J.A. and Varley, N., 2008. Fumarole monitoring with a handheld infrared camera; Volcan de Colima, Mexico, 2006-2007. Journal of Volcanology and Geothermal Research, 177(4), 911-924.

Sutton, M.A., Orteu, J.-J. and Schreier, H., 2009. Image Correlation for Shape, Motion and Deformation Measurements: Basic Concepts,Theory and Applications. Springer, New York, 342 pp.

Thiele, S.T., Varley, N. and James, M.R., 2017. Thermal photogrammetric imaging: A new technique for monitoring dome eruptions. Journal of Volcanology and Geothermal Research, 337, 140-145.

Vallance, J.W., Schneider, D.J. and Schilling, S.P., 2008. Growth of the 2004-2006 lava-dome complex at Mount St. Helens, Washington. U S Geological Survey Professional Paper, Report: P 1750, 169-208.

Varley, N.R., Connor, C.B. and Komorowski, J.-C., 2019. Volcán de Colima - Managing the Threat. Springer, Berlin, 1-366 pp.

Voight, B., 2000. Structural stability of andesite volcanoes and lava domes. Philosophical Transactions of the Royal Society of London, 358(1770), 1663-1703.

Wadge, G., Cole, P., Stinton, A., Komorowski, J.C., Stewart, R., Toombs, A.C. and Legendre, Y., 2011. Rapid topographic change measured by high-resolution satellite radar at Soufriere Hills Volcano, Montserrat, 2008-2010. Journal of Volcanology and Geothermal Research, 199(1-2), 142-152.

Wadge, G., Ryan, G. and Calder, E.S., 2009. Clastic and core lava components of a silicic lava dome. Geology, 37(6), 551-554.

Walter, T.R., 2011. Low cost volcano deformation monitoring: Optical strain measurements and application to Mount St. Helens data. Geophysical Journal International, 186(2), 699–705.

Walter, T.R., Legrand, D., Granados, H.D., Reyes, G. and Arambula, R., 2013a. Volcanic eruption monitoring by thermal image correlation: Pixel offsets show episodic dome growth of the Colima volcano. J Geophys Res-Sol Ea, 118(4), 1408-1419.

Walter, T.R., Ratdomopurbo, A., Subandriyo, Aisyah, N., Brotopuspito, K.S., Salzer, J. and Luhr, B., 2013b. Dome growth and coulee spreading controlled by surface morphology, as determined by pixel offsets in photographs of the 2006 Merapi eruption. Journal of Volcanology and Geothermal Research, 261, 121-129.

Walter, T.R., Subandriyo, J., Kirbani, S., Bathke, H., Suryanto, W., Aisyah, N., Darmawan, H., Jousset, P., Luehr, B.G. and Dahm, T., 2015. Volcano-tectonic control of Merapi's lava dome splitting: The November 2013 fracture observed from high resolution TerraSAR-X data. Tectonophysics, 639, 23-33.

Yamashina, K., Matsushima, T. and Ohmi, S., 1999. Volcanic deformation at Unzen, Japan, visualized by a time-differential stereoscopy. Journal of Volcanology and Geothermal Research, 89, 73-80.

Yokoyama, I., 2005. Growth rates of lava domes with respect to viscosity of magmas. Ann Geophys-Italy, 48(6), 957-971.

Zimmer, M., Walter, T.R., Kujawa, C., Gaete, A. and Franco-Marin, L., 2017. Thermal and gas dynamic investigations at Lastarria volcano, Northern Chile. The influence of precipitation and atmospheric pressure on the fumarole temperature and the gas velocity. Journal of Volcanology and Geothermal Research, 346, 134-140.

Zobin, V.M., Arambula, R., Breton, M., Reyes, G., Plascencia, I., Navarro, C., Tellez, A., Campos, A., Gonzalez, M., Leon, Z., Martinez, A. and Ramirez, C., 2015. Dynamics of the January 2013-June 2014 explosive-effusive episode in the eruption of Volcan de Colima, Mexico: insights from seismic and video monitoring. Bulletin of Volcanology, 77(4).

Zorn, E.U., Rowe, M.C., Cronin, S.J., Ryan, A.G., Kennedy, L.A. and Russell, J.K., 2018. Influence of porosity and groundmass crystallinity on dome rock strength: a case study from Mt. Taranaki, New Zealand. Bulletin of Volcanology, 80(4).

## FIGURE CAPTIONS

**Figure 1:** Satellite image of Volcán de Colima and the location of the camera and the seismic stations referred to in this work. (a) Volcán de Colima is located 5-6 km south of the observatory post at Nevado de Colima. The closest seismic station is indicated by a star. Camera location (DSLR) and TerraSAR-X viewing geometries (line of sight) are indicated by symbols. (b) Topographic profile from north to south, showing the field-of-view of the camera, and a sketch of the TerraSAR-X (TSX) radar satellite view (not to scale). (c) View from the web camera that is used for monitoring purposes, and (d) close view shown by the high-resolution DSLR time-lapse camera used. (e) Close-up view of areas shown in Figures 3-5.

**Figure 2:** Data used in this study as a function of time. Seismic records show the occurrence of four significant trend changes slightly preceding four explosions in early 2013 due to precursory long-period events (red vertical lines) illustrated by event counts per hour (red trend line, y-axis on left). TerraSAR-X satellite radar images were available every 11 days (black crosses). Available time-lapse camera images are shown as black points (clear daytime images) and grey points (cloudy and night images). See the methods section for details.

**Figure 3:** Spotmode TerraSAR-X amplitude image views of the summit region of Volcán de Colima, from January – April 2013. Radar coordinates, ascending track (W is left, E is right, S is up, N is down). Acquisition dates are given for each image. The combination of three images allows derivation of a composite map, and the respective red, green and blue channels are indicated as R-G-B. See the text for details.

**Figure 4:** High-resolution time-lapse camera record from a ~6 km distance. The initial phase of activity and first crater formation (a-b). The old dome shows a fumarole on its western side (right in image). After a snowfall event, new ring-shaped degassing features appear (d-f). Two days later, the first explosion occurred on 6 January 2013, with dimensions exactly matching the degassing ring. Signs of vigorous degassing disappear afterwards.

**Figure 5:** High-resolution time-lapse camera record from a ~6 km distance. The 6 January 2013 explosion crater (crater-1) widens by an explosion on 11 January (crater-2), partially overlapping but migrating eastward. New fumarole activity appeared on its east before the third explosion occurred on 13 January, again migrating further eastward. The fourth explosion on 29 January is not seen by new crater excavation, but by the presence of a major bomb. Numbers in circles indicate chronologically numbered crater, width of the horizontal indicates maximum crater width as seen in the camera.

**Figure 6:** High-resolution time-lapse camera record from a ~6 km distance showing dome extrusion. The first dome becomes visible on 14-Feb. (a) which then grows vertically (b, c) and then predominantly laterally (d, e) until the western crater rim (craters 1 and 2) is overflowing (f), oversteepening (g) and develops into a lava flow (h) with small collapses leading to rockfalls and small block and ash flows.

**Figure 7:** Digital image correlation results showing the growth of the dome, initially dominated by vertical growth (a, b). At a height of approximately 25 m, the dominantly vertical growth regime changes into a dominantly lateral growth regime. Occasional short-term subsidence of the dome is observed, possibly associated with

block rotation or spreading (c). Continued growth grades into a lateral direction of magma extrusion forming lava flows (d).

**Figure 8:** Growth of the dome in the lateral and vertical directions, and volume estimations. Measurements at the east side of the dome are shown as grey symbols (squares), and measurements at the west side of the dome are shown as black symbols (circles). (a) Both sides of the dome show vertical growth changing into a more dominant lateral growth domain after an ~25 m height is reached. (b) The volume of the eastern dome is growing constantly, whereas the volume of the western dome strongly increases the lava flow, and crater overflow develops.

**Figure 9:** Comparison of dome growth camera observations (green curves) and distinct element models (red curves). The lateral (left Y-axis) and vertical dome growth (right Y-axis) are shown separately. The east and west sides of the lateral dome growth are shown in grey, average in green. The initially steep vertical growth and subsequent dominantly lateral growth can be well explained by models. The X-axis shows date for observations, and normalized time for models. The change in slope from the graph is explained by the dome reaching a critical strength threshold.

**Figure 10**: Summary sketch of the chronology of the events described in the text, based on constraints from seismic data (S), camera data (C) and TerraSAR-X data (T). Pre-eruptive deformation based on interferometric processing of the TerraSAR-X data (Salzer et al., 2014; Salzer et al., 2017).

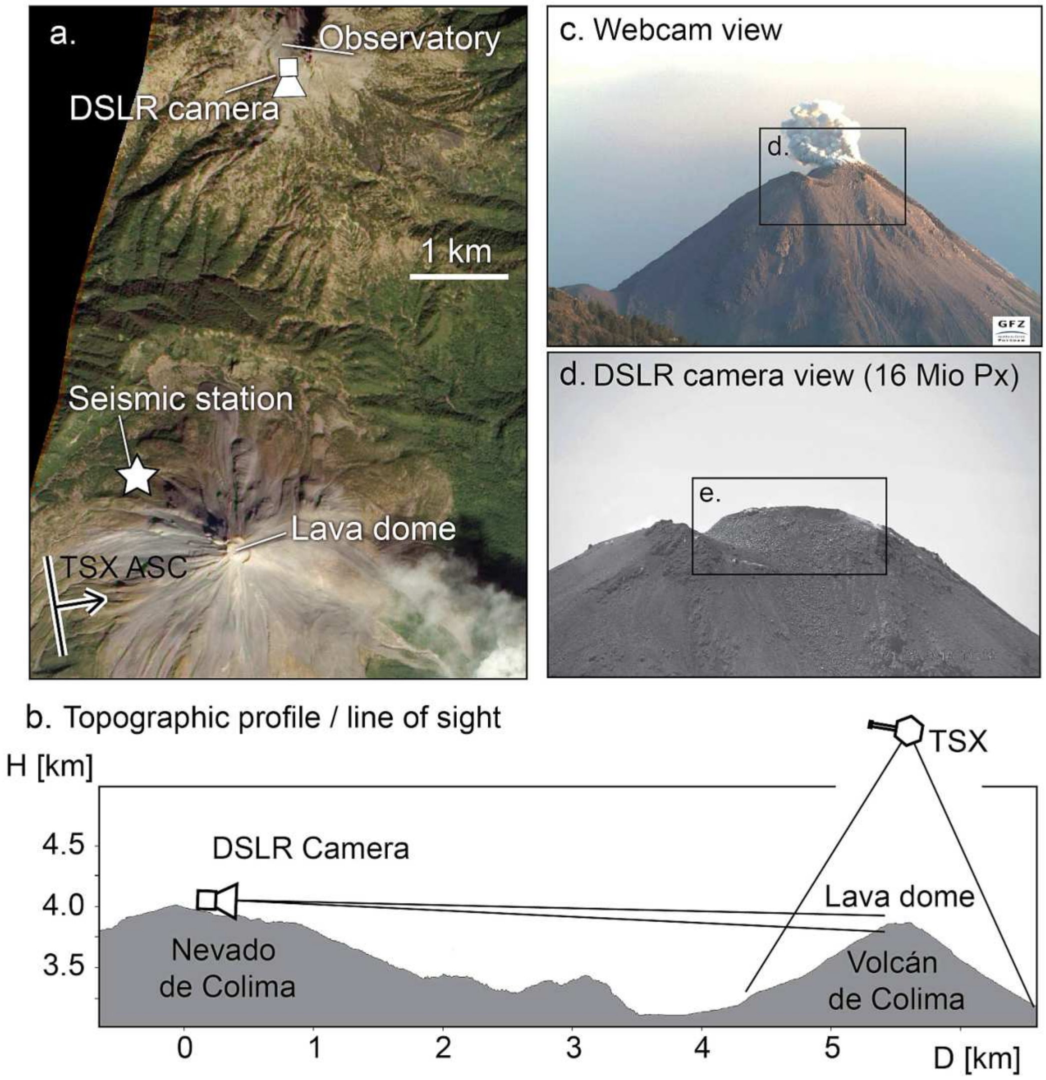


1015

1016

1017 Figure 1

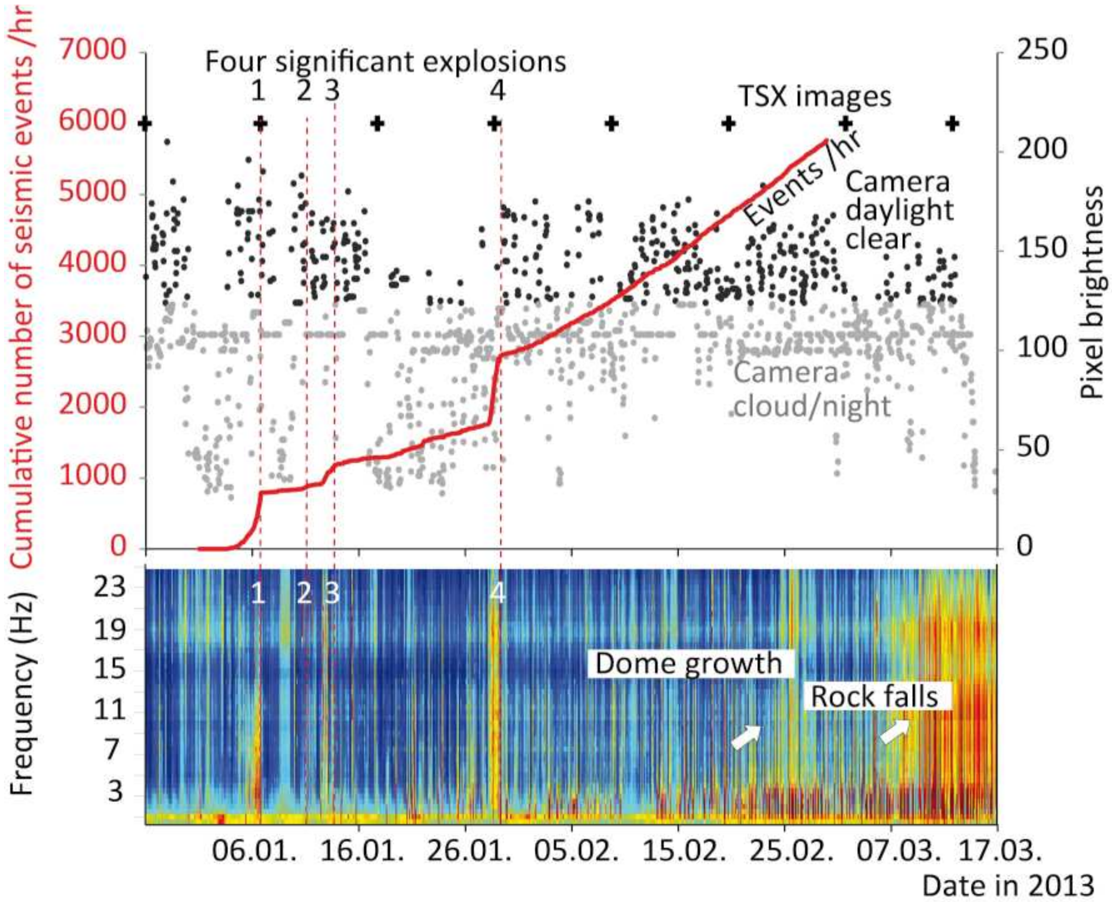
Cumulative number of seismic events /hr
7000
6000
5000
4000
3000
2000
1000
0
Four significant explosions
1
2
3
4
TSX images
Events /hr
Camera daylight clear
Camera cloud/night
250
200
150
100
50
0
Pixel brightness
Frequency (Hz)
23
19
15
11
7
3
Dome growth
Rock falls
06.01.
16.01.
26.01.
05.02.
15.02.
25.02.
07.03.
17.03.
Date in 2013

Figure 2

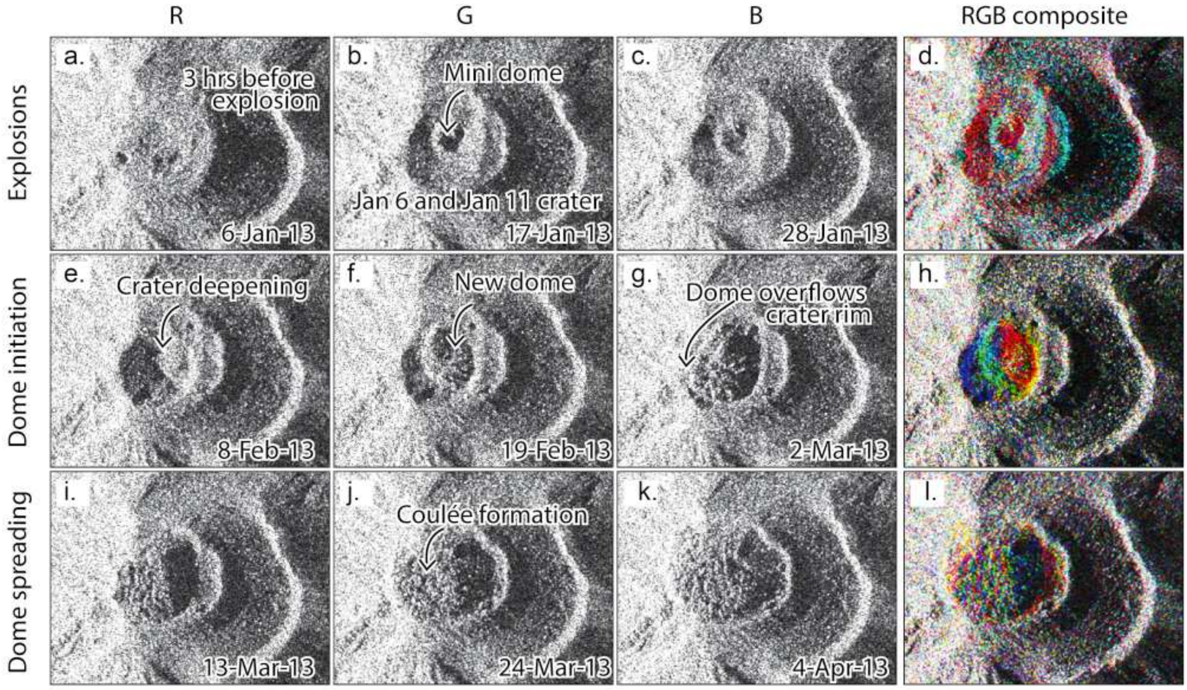
R
G
B
RGB composite
Explosions
Dome initiation
Dome spreading
a.
3 hrs before explosion
6-Jan-13
b.
Mini dome
Jan 6 and Jan 11 crater
17-Jan-13
c.
28-Jan-13
d.
e.
Crater deepening
8-Feb-13
f.
New dome
19-Feb-13
g.
Dome overflows crater rim
2-Mar-13
h.
i.
13-Mar-13
j.
Coulée formation
24-Mar-13
k.
4-Apr-13
l.

Figure 3

January 6, 2013 explosion: Fumarole precursors and first crater formation

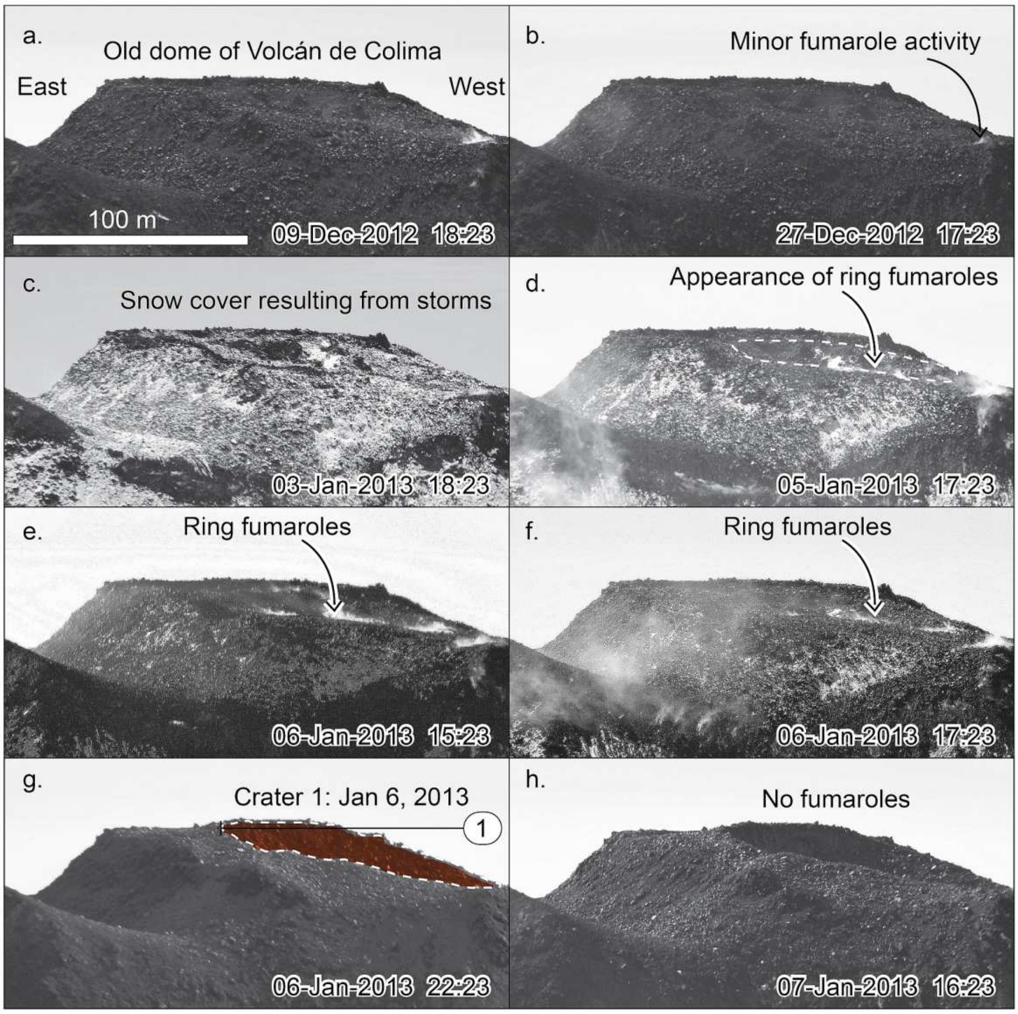


Figure 4

January explosions: Nested crater formation and migration to the east

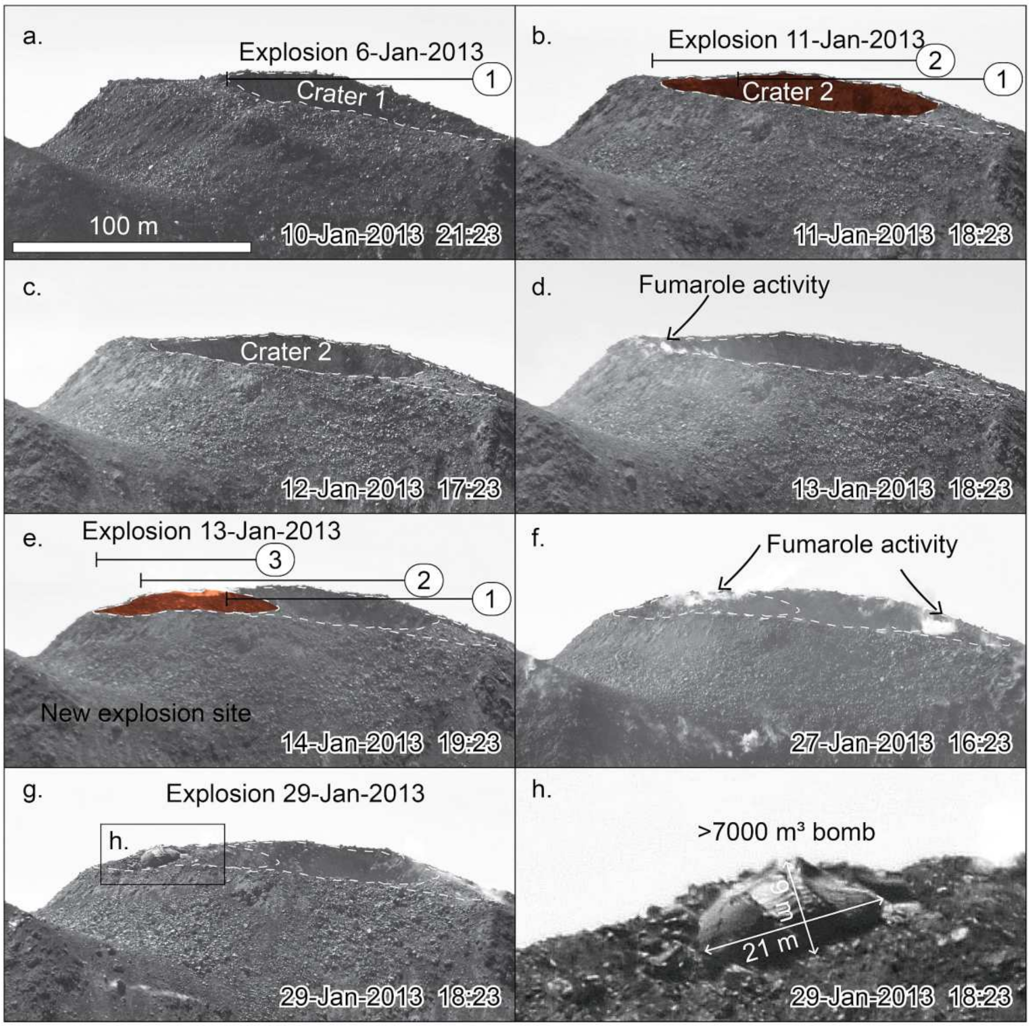


Figure 5

February, 2013: Dome growth and lateral spreading

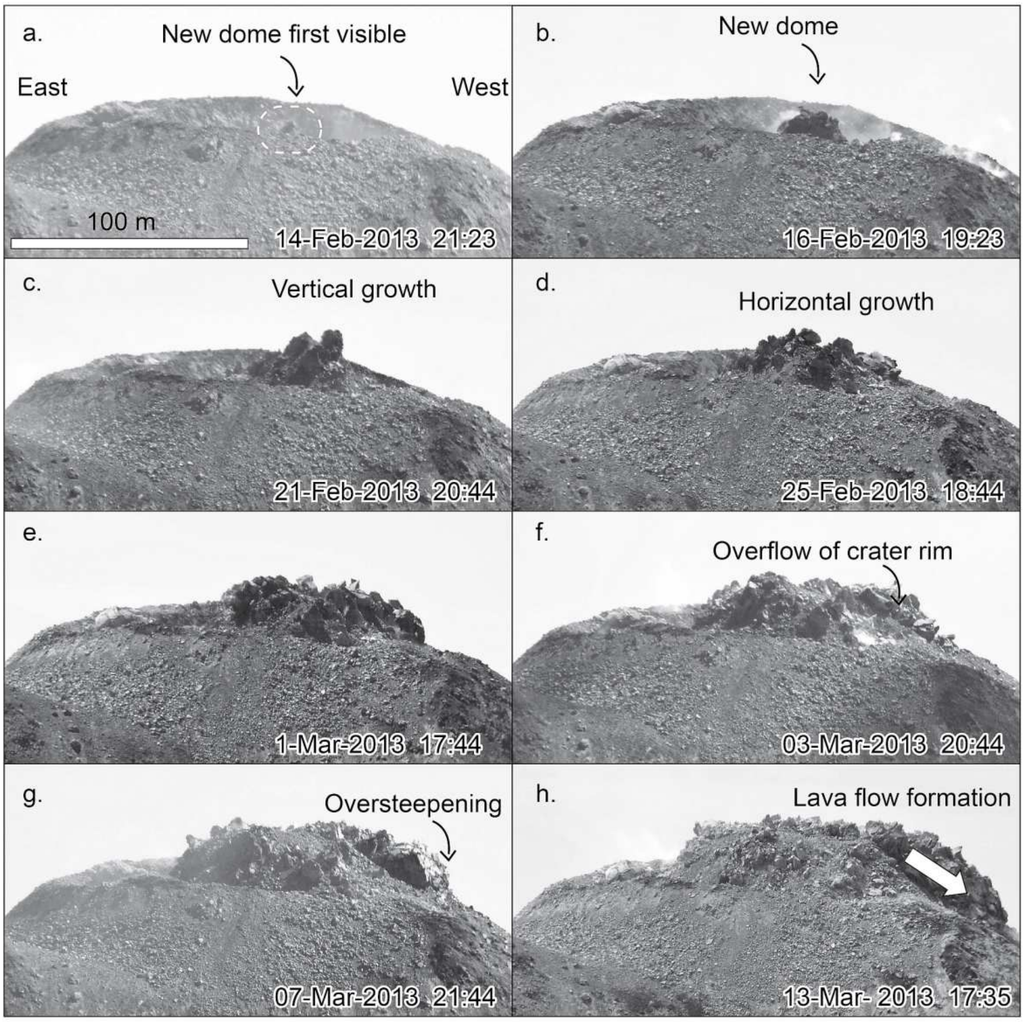


Figure 6

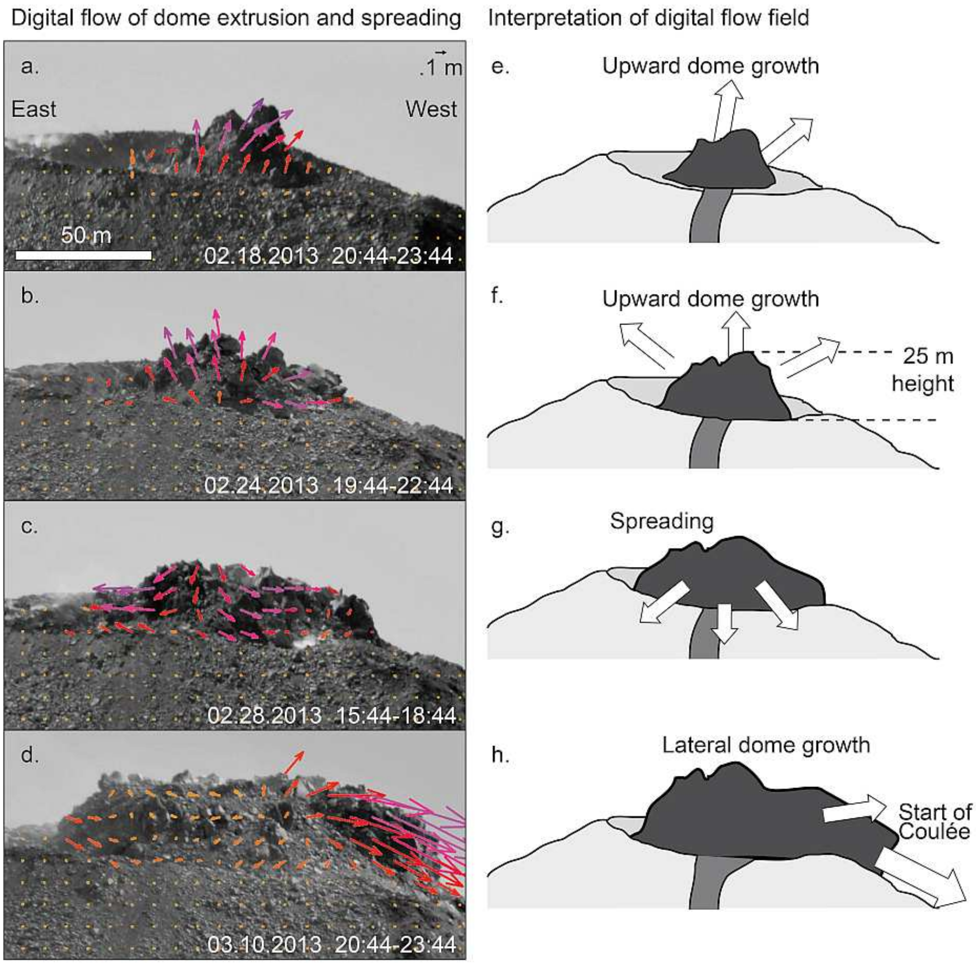
Digital flow of dome extrusion and spreading
Interpretation of digital flow field
a.
.1 m
East
West
50 m
02.18.2013 20:44-23:44
b.
02.24.2013 19:44-22:44
c.
02.28.2013 15:44-18:44
d.
03.10.2013 20:44-23:44
e.
Upward dome growth
f.
Upward dome growth
25 m
height
g.
Spreading
h.
Lateral dome growth
Start of
Coulée

Figure 7

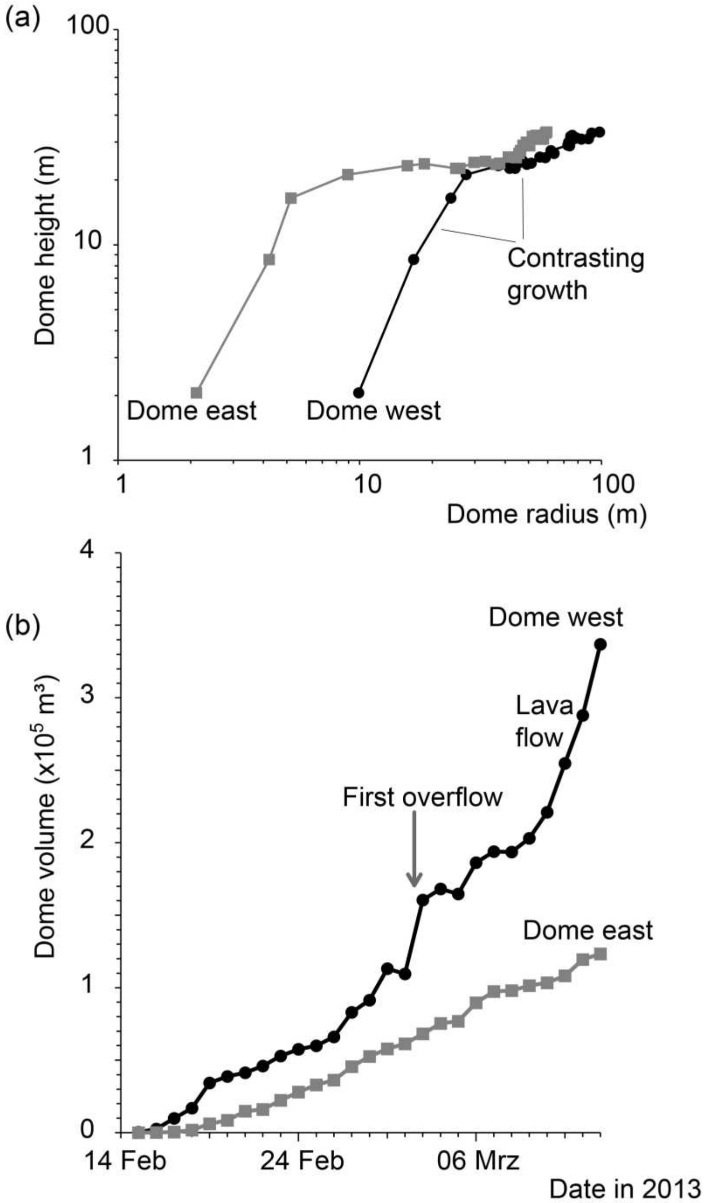
(a)
100
10
1
Dome height (m)
Contrasting growth
Dome east
Dome west
1
10
100
Dome radius (m)
4
3
2
1
0
(b)
Dome volume (x10$^5$ m³)
Dome west
Lava flow
First overflow
Dome east
14 Feb
24 Feb
06 Mrz
Date in 2013

Figure 8

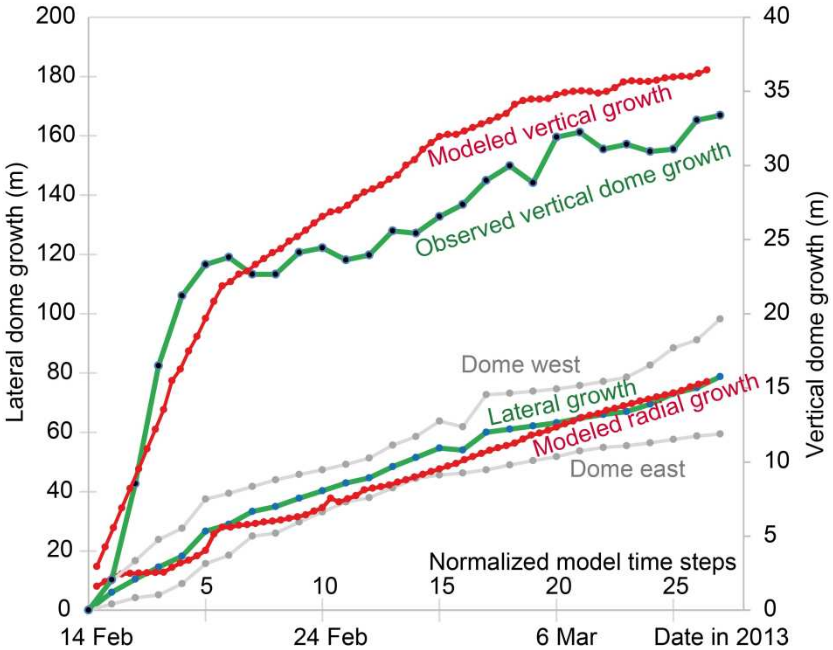


Figure 9

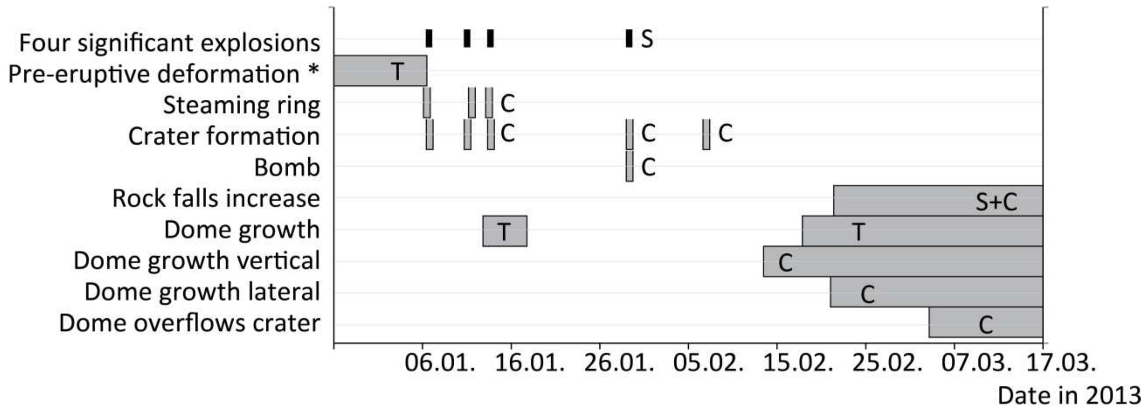


Figure 10.

## Appendix Material

### 1. Model setup

The model is initialized with lava material in the conduit and topography that matches the observed topography from the high resolution time-lapse camera. For simplicity, the

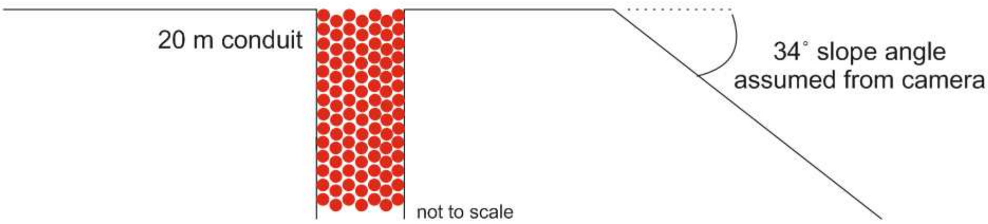


topography within the crater is assumed to be horizontal. A vertical velocity is given to all material in the conduit to simulate extrusion.

**Figure A1.** Conceptual diagram of model setup.

The surface boundaries in this instance are given purely frictional properties. This ensures, for example, that particles do not endlessly roll downhill. There are otherwise no cohesive bond properties between balls and boundaries.

In order to equate the timescales between the observations and the model scenario, we use the start of extrusion as Time 0 in each case, and the point at which the dome reaches the break in slope as Time 1. We then adopt normalized time between these two end points.

### 2. Material Calibration

Material behavior is controlled in PFC by the micro-properties that exist at the contacts between particles. These micro-properties are not equivalent to the macro-properties of the material as a whole. Therefore, a calibration procedure is required to determine the micro-properties that result in the same macro-behavior of the model material to the real material in the laboratory (Figure A2).

We then iteratively adapt these parameters to fit the modelled dome extrusion to the observational data. Once the two datasets match, we can use the parameters to back-analyze the required intact rock strength (Figure A3). The parameters for each material are shown in Table A1.

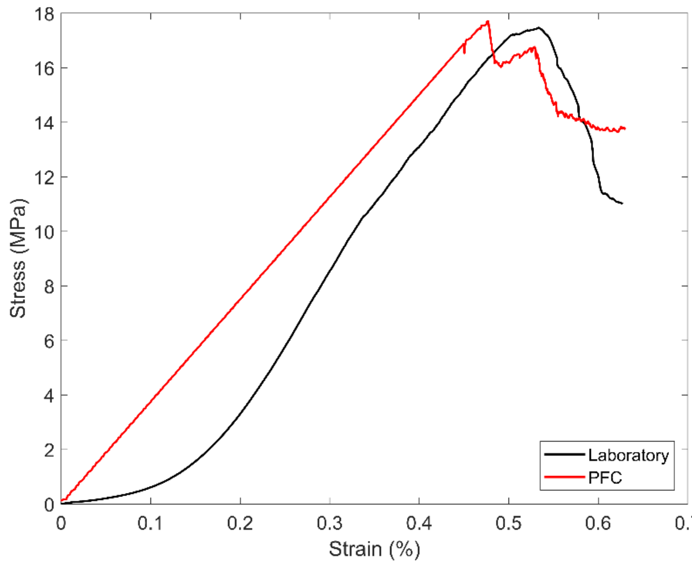


**Figure A2**. Stress-strain curves showing the macro-scale behaviour from the laboratory material (Heap et al. 2014) and the PFC material. Peak stress of laboratory tested material = 17.5 MPa, Young's modulus = 8.1 GPa.

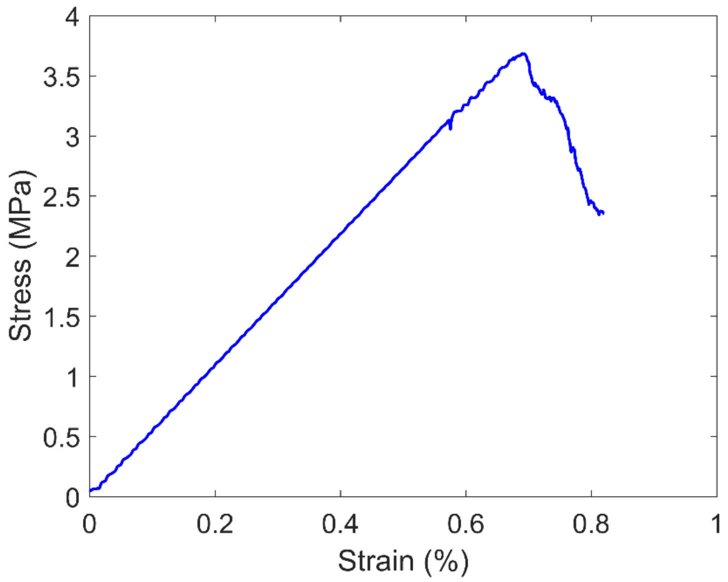


**Figure A3.** Stress-strain response from the PFC material that is required to fit the observational data from the time-lapse camera at Colima. Peak stress = 3.7 MPa, Young's modulus = 5.5 GPa.

| | *Fitted to laboratory data* | *Fitted to observations* |
|---|---|---|
| *Shear stiffness* | 1.25e9 Pa | 1e9 Pa |
| *Normal stiffness* | 1.25e9 Pa | 1e9 Pa |
| *Cohesion* | 2.7e7 Pa | 5e6 Pa |
| *Friction coefficient* | 0.84 | 0.84 |
| *Friction angle* | 38˚ | 38˚ |
| *Bond modulus* | 1.1e10 Pa | 1.6e9 Pa |

**Table A1.** PFC parameters for the talus material in (a) the material that is calibrated to sample-scale laboratory tests of Colima samples (Heap et al. 2014) and (b) the material that is used to fit the observational data and allows us to back-analyse rock strength.

## 3. 3D correction

Complex models in PFC in 3D are very computationally expensive, and so the models in this paper are presented in 2D. However, there are limitations to comparing the 2D method with the 3D observational data. To overcome this, we perform a calibration of the PFC data. By extruding material using the same model parameters in both 2D and 3D, we see that in 2D, the model gains more height as it cannot spread laterally in several directions (Figure A4). This results in an overestimate of height (by approximately 33%) and an underestimate in width (by approximately 33%). We apply these correction factors to the data presented in the paper.

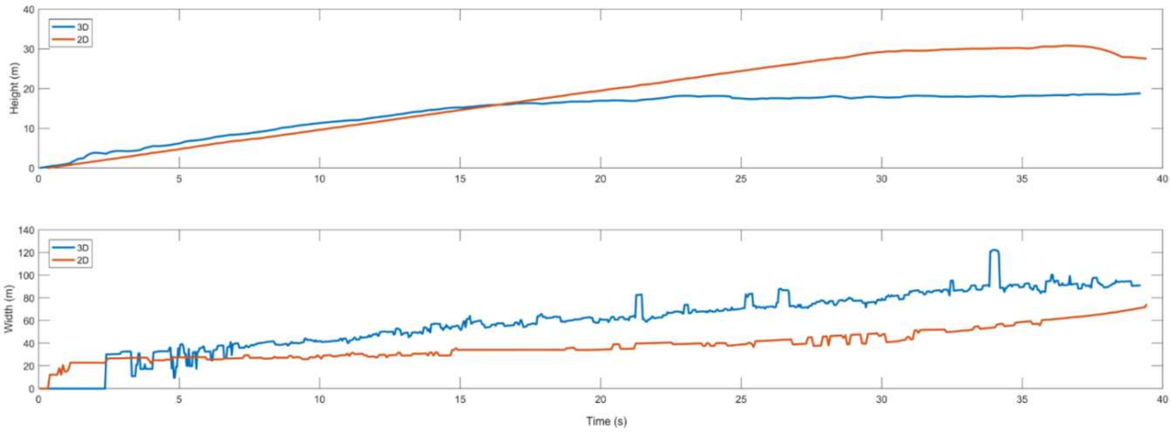


**Figure A.4.** Height and width evolution of a PFC dome in 2D and 3D.